Available online at www.sciencedirect.com
ScienceDirect
International Journal of Multiphase Flow 34 (2008) 748–766
International Journal of Multiphase Flow
www.elsevier.com/locate/ijmulflow

A filtered mass density function approach for modeling separated two-phase flows for LES II: Simulation of a droplet laden temporally developing mixing layer

M.D. Carrara [1], P.E. DesJardin *

Department of Mechanical and Aerospace Engineering, University at Buffalo, The State University of New York, Buffalo, NY 14260-4400, United States

Received 19 January 2007; received in revised form 1 February 2008

Abstract

A two-phase velocity-scalar filtered mass density function (TVSFMDF) formulation developed for large eddy simulation (LES) is applied to a temporally developing counter-current mixing layer seeded with water droplets. Closure models for both the dispersed and carrier phases are developed and implemented that are self-consistent with the original TVSFMDF mathematical formulation developed by Carrara and DesJardin. Several simulation cases are conducted to examine the sensitivity of both evaporating and non-evaporating droplet dispersion on various levels of subgrid scale (SGS) modeling approximation – highlighting the importance of variations in composition space in the phase-coupling terms.

Keywords: Two-phase flow; FDF methods; Temporal mixing layer; LES; Droplet gas flow

1. Introduction

The interaction between the carrier phase and particulate phase on the dispersion and evaporation/reaction of dilute particulate–gas two-phase flows is extremely important in many natural and technological flows. Ideally, the best tool for simulation and analysis of a fully-coupled gas-reactive particulate dispersed two-phase flow is direct numerical simulation (DNS), however, the number of degrees of freedom needed to adequately describe most systems is such that a true DNS would not be practical. As an alternative, large eddy simulation (LES) approaches may be pursued for which large-scale features of the flow are simulated while small-scale features are modeled. The phase-averaged equations for LES of a separated two-phase flow have been formulated by several authors (Oefelein and Yang, 1996; Sirignano, 2005; Bellan, 2005) and may be classified into two general categories. The first is where the governing equations for each phase are spatially filtered to obtain phase-averaged LES equations. Commuting the spatial and temporal derivatives with the filtering operation results in surface integrals that account for the phase-coupling between each phase (Oefelein and Yang, 1996; Sirignano, 2005). In the second approach, it is *assumed* that the influence of the droplet field, for example, on the gas-phase system may be first approximated as a point approximation resulting in so called "exact" gas-phase conservation equations (Okong'o and Bellan, 2004). These equations are then subsequently filtered resulting in additional SGS terms that must be modeled. The latter approach may be also thought of as two subsequent applications of a filtering operation. The first filtering operation uses a much smaller filter width than the second and has a scale associated with an isolated droplet

* Corresponding author. Tel.: +1 716 645 2593x2314; fax: +1 716 645 3875.
E-mail address: ped3@eng.buffalo.edu (P.E. DesJardin).
[1] Present address: Applied Physics Division, Los Alamos National Laboratory, Los Alamos, NM 87545, United States.

0301-9322/$ - see front matter © 2008 Elsevier Ltd. All rights reserved.
doi:10.1016/j.ijmultiphaseflow.2008.02.003

for which the influence of the turbulent flow field is neglected. In this limit the second-order correlations associated with the filtering of non-linear convection terms vanish (Carrara and DesJardin, 2006). A second filtering operation is then applied using a much larger filter width for which the influence of turbulence may be introduced. In either approach for developing the phase-filtered LES equations, the main challenge for closing the system of equations is prescribing a closure model for the phase-coupling terms (PCT). Recent *a priori* DNS studies of droplet laden temporally developing flows have highlighted that large PCT errors may occur if insufficient computational parcels are used to represent the variation in the SGS composition, even for very low mass loadings (Miller and Bellan, 2000). Similar to the problem of modeling filtered chemical reaction source terms for a single-phase flow, it appears then that directly closing the PCT for two-phase flows using local filtered information will most likely result in erroneous results.

As a promising alternative to moment based methods, probability density function (PDF) approaches have been successful applied for single-phase flows over the last 30 years in the context of Reynolds averaged Navier–Stokes (RANS) formulations (Lundgren, 1967; Pope, 1985; Pope, 1976; Dopazo and O'Brien, 1976; O'Brien, 1980; Rhodes, 1975; Bilger et al., 1976; Janicka et al., 1979; Givi, 1989; Fox, 2003) and filtered density function (FDF) approaches in the context of LES (Colucci et al., 1998; Zhou and Pereira, 2000; Jaberi et al., 1999; Givi, 2003). In PDF/FDF approaches, subgrid scale modeling is probabilistic in nature, and the main advantage of these approaches is that source terms in the gas phase appear in closed form. Two-phase probability density function (PDF) methods have also recently been formulated and successfully applied for dispersed two-phase flows (Minier and Peirano, 2001; Zhou and Pereira, 2000; Zhu, 1996). Hybrid LES/PDF methods have also been used for spray simulations. In this approach the PDF of the droplet field represents an ensemble of droplets while the properties of the LES are derived from spatial filtering principles. While it is certainly possible to conduct simulations using such a hybrid approach (Apte et al., 2003), it is not clear that these two concepts are compatible and the interpretation the results is not straight forward.

Most recently, Carrara and DesJardin have extended the FDF approach to separated two-phase flows (Carrara and DesJardin, 2006). In this development, a transport equation for the two-phase velocity-scalar filtered mass density function (TVSFMDF) is derived starting from the instantaneous governing equations for each phase. Unclosed terms in the transport equation may be categorized in terms of conditionally filtered quantities within a phase and on the phase interface (Carrara and DesJardin, 2006). The closure of these terms are in general problem specific, however, it was shown that they may be directly related to the functional form of closures commonly used phase-averaged averaged LES equations. In this study, the TVSFMDF formulation is applied for an evaporating water droplet–gas system where unclosed conditionally averaged PCT that appear in the transport are closed in the LES context. The resulting equations are solved using a full particle based Monte-Carlo solution procedure for application to a two-dimensional temporally developing mixing layer.

The remainder of this article is organized as follows: in Section 2 the two-phase FMDF formulation is first summarized. Closure models are then presented in Section 3 for both the gas and droplet phases. Section 4 summarizes the numerical procedure use to solve the system of stochastic differential equations followed by Section 5 that present results and discussion. Section 6 summarizes the major findings from this study.

2. Unclosed two-phase FMDF transport equation

The TVSFMDF, F_L, contains the one-point statistical information for both phases of the flow. The TVSFMDF may be defined in terms of the spatially filtered two-phase fine-grain density function, ξ (Carrara and DesJardin, 2006):

$$\begin{aligned} F_L(\mathbf{u}_k, \Psi_{\alpha,k}; \mathbf{x}, t) &\equiv \langle \xi(\mathbf{u}_k, \Psi_{\alpha,k}, \mathbf{v}_k, \zeta, \psi_{\alpha,k}, \gamma; \mathbf{x}, t) \rangle \\ &= \sum_{k=1}^{2} \int_{\infty} \mathrm{d}^3 x' \rho_k(\mathbf{x}', t) G(\mathbf{x}' - \mathbf{x}) \phi_k(\mathbf{x}', t) \\ &\quad \times \xi_k(\mathbf{u}_k, \Psi_{\alpha,k}, \mathbf{v}_k, \zeta, \psi_{\alpha,k}, \gamma; \mathbf{x}', t), \end{aligned} \tag{1}$$

where the two-phase fine-grain density function for velocity $\mathbf{u}_k$ and field scalars, $\Psi_{\alpha,k}$ may be defined for a separated two-phase flow following Carrara and DesJardin (2006). Alternatively, the two-phase fine-grain density function may be defined to include phase interface information as follows:

$$\begin{aligned} &\xi(\mathbf{u}_\mathrm{g}, \mathbf{u}_\mathrm{p}, \mathbf{v}_\mathrm{g}, \mathbf{v}_\mathrm{p}, \Psi_{\alpha,\mathrm{g}}, \Psi_{\alpha,\mathrm{p}}, \psi_{\alpha,\mathrm{g}}, \psi_{\alpha,\mathrm{p}}, \gamma, \zeta; \mathbf{x}, t) \\ &\quad \equiv \sum_{k=1}^{2} \phi_k(\mathbf{x}, t) \prod_{i=1}^{3} \delta[v_{k,i}(\mathbf{x}, t) - u_{k,i}] \\ &\qquad \times \prod_{i=1}^{\sigma} \delta[\psi_{\alpha,k}(\mathbf{x}, t) - \Psi_{\alpha,k}] \delta[\gamma(\mathbf{x}, t) - \zeta]. \end{aligned} \tag{2}$$

The advantage of including the phase interface function, γ, in the composition phase-space is that the decomposition of the two-phase-filtered density function into marginals for each phase is more straight forward for practical application (Zhu et al., 2000). In Eq. (2) δ denotes a Dirac delta distribution and $\phi_k(\zeta)$ is a phase indicator function which is defined as 1 is phase k and 0 otherwise. The variables $\Psi_{\alpha,k}, \mathbf{u}_k$ and ζ are sampled values for the corresponding random variables $\psi_{\alpha,k}, \mathbf{v}_k$ and γ for the composition (*i.e.*, temperature, species mass fraction, and interface location, *etc.*) and velocity, respectively, at a given spatial location $\mathbf{x}$ and time t. The subscripts "g" and "p" represent the property of the gas and liquid phases, respectively. Assuming a low Mach number approximation and simple diffusion

with equal diffusivities then the transport equations governing the gas and liquid phase enthalpy (h) and species mass fraction (Y_β) may be expressed in a general form

$$\frac{\partial}{\partial t}(\rho\psi) + \nabla\cdot(\rho\psi\mathbf{v}) = -\nabla\cdot\mathbf{J} + \rho S, \tag{3}$$

where $\psi(= Y_\beta, h)$ and $\mathbf{J} = -\Gamma\nabla\psi(= -\rho\mathscr{D}_m\nabla Y_\beta, -\mu/Sc\nabla h)$ where Sc is the Schmidt number, μ is the molecular viscosity and $\mathscr{D}_m$ is the diffusion coefficient. Following the development of Carrara and DesJardin, a transport equation for F_L may be derived by first differentiating, ξ, followed by the substitution in Eq. (3) and momentum conservation, and finally filtering the resulting equation to yield the following transport equation (Carrara and DesJardin, 2006; Zhu et al., 2000):

$$\begin{aligned}
&\frac{\partial F_L}{\partial t} + \frac{\partial}{\partial \mathbf{x}}[\langle\phi_g\mathbf{v}_g|_{\gamma\leqslant 0^-}\rangle F_L^g] + \frac{\partial}{\partial \mathbf{x}}[\langle\phi_p\mathbf{v}_p|_{\gamma\geqslant 0^+}\rangle F_L^p] \\
&\quad = -\frac{\partial}{\partial \mathbf{u}_g}\left[\left\langle \phi_g\left(-\frac{1}{\rho_g}\nabla P_g + \frac{1}{\rho_g}\nabla\cdot\underset{\sim g}{\boldsymbol{\tau}} + \mathbf{f}_g\right)|_{\gamma\leqslant 0^-}\right\rangle F_L^g\right] \\
&\qquad -\frac{\partial}{\partial \mathbf{u}_p}\left[\left\langle \phi_p\left(-\frac{1}{\rho_p}\nabla P_p + \frac{1}{\rho_p}\nabla\cdot\underset{\sim p}{\boldsymbol{\tau}} + \mathbf{f}_p\right)|_{\gamma\geqslant 0^+}\right\rangle F_L^p\right] \\
&\qquad -\frac{\partial}{\partial \Psi_{\alpha,g}}\left[\left\langle \phi_g\left(-\frac{1}{\rho_g}\nabla\cdot\mathbf{J}_{\alpha,g} + S_{\alpha,g}\right)|_{\gamma\leqslant 0^-}\right\rangle F_L^g\right] \\
&\qquad -\frac{\partial}{\partial \Psi_{\alpha,p}}\left[\left\langle \phi_p\left(-\frac{1}{\rho_p}\nabla\cdot\mathbf{J}_{\alpha,p} + S_{\alpha,p}\right)|_{\gamma\geqslant 0^+}\right\rangle F_L^p\right] \\
&\qquad + \langle\Pi_g|_{\gamma=0^-}\rangle F_L^g + \langle\Pi_p|_{\gamma=0^+}\rangle F_L^p \\
&\qquad + \frac{\partial}{\partial\zeta}\left[\left\langle(\mathbf{v}_p - \mathbf{v}^I)\cdot\nabla\phi_p|_{\zeta=0^+}\right\rangle F_L^p\right] + \frac{\partial}{\partial\zeta}[\langle(\mathbf{v}_g - \mathbf{v}^I) \\
&\qquad \cdot\nabla\phi_g|_{\zeta=0^-}\rangle F_L^g].
\end{aligned} \tag{4}$$

In Eq. (4) terms are conditionally averaged by phase where $\gamma(\zeta)$ is the function describing the phase interface at spatial location $\mathbf{x}$ at time t (Carrara and DesJardin, 2006). The conditionally averaged quantities are defined such that $\gamma \geqslant 0^+$ and $\gamma \leqslant 0^-$ correspond to averages within the particle phase and within the gas phase, respectively. Note that $\gamma = 0^+$ and $\gamma = 0^-$ correspond to averages on the phase interface approached from the particle and gas phases, in that order (Carrara and DesJardin, 2006). The terms $\mathbf{v}, \rho, P$ and $\mathbf{f}$ are the velocity, density, pressure and body force terms, respectively. The tensor $\boldsymbol{\tau}$ is the deviatoric part of the Cauchy stress tensor. The terms containing $\Pi_k(= \partial\phi_k/\partial t + \nabla\phi_k\cdot\mathbf{v}_k)$ are interphase volumetric conversion terms. These terms are small for a low particle loading and therefore will be neglected. Discussion of when it is and is not appropriate to disregard interphase conversion terms may be found in Carrara and DesJardin (2006). It should be noted that Eq. (4) is not a simple linear combination of two single-phase FMDF transport equations; assumptions about the nature of the interaction between the respective phases must be taken in order to cleanly extract the marginal FMDF transport equations in each phase.

Multiplying Eq. (4) by the phase indicator function, ϕ_j, results in the marginal VSFMDF: $F_L^j(\mathbf{u}_k, \Psi_{\alpha,k}, \zeta; \mathbf{x}, t) = \phi_j(\gamma)F_L(\mathbf{u}_k, \Psi_{\alpha,k}, \zeta; \mathbf{x}, t)$. The last four terms on the r.h.s. of Eq. (4) involve phase coupling due to volumetric phase conversion and mass transfer processes (Carrara and DesJardin, 2006). Assuming low particle loading, these terms may be safely neglected resulting in the following marginal VSFMDF for the gas-phase system:

$$\begin{aligned}
&\frac{\partial F_L^g}{\partial t} + \frac{\partial}{\partial \mathbf{x}}[\langle\phi_g\mathbf{v}_g|_{\gamma\leqslant 0^-}\rangle F_L^g] \\
&\quad = -\frac{\partial}{\partial \mathbf{u}_g}\left[\left\langle \phi_g\left(-\frac{1}{\rho_g}\nabla P_g + \frac{1}{\rho_g}\nabla\cdot\underset{\sim g}{\boldsymbol{\tau}} + \mathbf{f}_g\right)|_{\gamma\leqslant 0^-}\right\rangle F_L^g\right] \\
&\qquad -\frac{\partial}{\partial \Psi_{\alpha,g}}\left[\left\langle \phi_g\left(-\frac{1}{\rho_g}\nabla\cdot\mathbf{J}_{\alpha,g} + S_{\alpha,g}\right)|_{\gamma\leqslant 0^-}\right\rangle F_L^g\right].
\end{aligned} \tag{5}$$

As can be seen in Eq. (5), transport of F_L^g is generated in configuration, velocity and scalar phase-spaces. Following Carrara and DesJardin (2006), standard conditional dissipation/diffusion decompositions can be applied to the conditional averages within each phase resulting in

$$\begin{aligned}
&\frac{\partial F_L^g}{\partial t} + \frac{\partial}{\partial \mathbf{x}}(\mathbf{u}_g F_L^g) \\
&\quad = \frac{\partial}{\partial \mathbf{x}}\left[\mu_g\frac{\partial(F_L^g/\widehat{\rho_g})}{\partial \mathbf{x}}\right] - \frac{\partial^2}{\partial \mathbf{u}_g\cdot\partial \mathbf{u}_g}[\langle\mu_g\phi_g\nabla\mathbf{v}_g\cdot\nabla\mathbf{v}_g|_{\gamma<0^-}\rangle \\
&\qquad \times(F_L^g/\widehat{\rho_g})] + \frac{\partial}{\partial \mathbf{x}}\left[\Gamma_{\alpha,g}\frac{\partial(F_L^g/\widehat{\rho_g})}{\partial \mathbf{x}}\right] - \frac{\partial^2}{\partial \mathbf{u}_g\partial\Psi_{\alpha,g}} \\
&\qquad \times[\langle\mu_g\phi_g\nabla\mathbf{v}_g\cdot\nabla\psi_{\alpha,g}|_{\gamma<0^-}\rangle(F_L^g/\widehat{\rho_g})] - \frac{\partial}{\partial\Psi_{\alpha,g}}[S_{\alpha,g}F_L^g] \\
&\qquad - \frac{\partial^2}{\partial\Psi_{\alpha,g}\partial\Psi_{\beta,g}}[\langle\phi_g\Gamma_{\alpha,g}\nabla\psi_{\alpha,g}\cdot\nabla\psi_{\beta,g}|_{\gamma<0^-}\rangle(F_L^g/\widehat{\rho_g})] \\
&\qquad + \frac{\partial}{\partial \mathbf{u}_g}\left[\left\langle\frac{1}{\rho_g}\nabla(\phi_g P_g)|_{\gamma<0^-}\right\rangle F_L^g\right] - \frac{\partial^2}{\partial\Psi_{\alpha,g}\partial \mathbf{u}_g} \\
&\qquad \times[\langle\phi_g\Gamma_{\alpha,g}\nabla\psi_{\alpha,g}\cdot\nabla\mathbf{v}_g|_{\gamma<0^-}\rangle(F_L^g/\widehat{\rho_g})] - \frac{\partial}{\partial \mathbf{u}_g}[\langle\phi_g\mathbf{f}_g|_{\gamma<0^-}\rangle F_L^g] \\
&\qquad + \frac{\partial}{\partial\Psi_{\alpha,g}}\left[\left\langle\frac{1}{\rho_g}\Gamma_{\alpha,g}\nabla\psi_{\alpha,g}^I\cdot\mathbf{e}_{n,g}^I a^I|_{\gamma=0^-}\right\rangle F_L^g\right] \\
&\qquad - \frac{\partial}{\partial \mathbf{u}_g}\left[\left\langle\frac{1}{\rho_g}P_g^I\mathbf{e}_{n,g}^I a^I|_{\gamma=0^-}\right\rangle F_L^g\right] + \frac{\partial}{\partial \mathbf{u}_g}\left[\left\langle\frac{1}{\rho_g}\underset{\sim g}{\overset{I}{\boldsymbol{\tau}}}\cdot\mathbf{e}_{n,g}^I a^I|_{\gamma=0^-}\right\rangle F_L^g\right]
\end{aligned} \tag{6}$$

for which additional terms appear involving the conditional average of quantities on the phase interface (*i.e.*, $\gamma = 0^+$ and $\gamma = 0^-$) involving the instantaneous interfacial surface area, $\mathbf{e}_k a^I \equiv \nabla\phi_k = \delta(\gamma)\nabla\gamma$. In Eq. (6) μ_g is the gas-phase molecular viscosity, P_g is the thermodynamic pressure, ρ is the mass density and $\Gamma_{\alpha,k}$ is the gradient flux transport coefficient for the transported scalar quantity $\psi_{\alpha,k}$ in phase k; that is, $\mathbf{J}_{\alpha,k} = \Gamma_{\alpha,k}\nabla\psi_{\alpha,k}$ for the flux $\mathbf{J}_{\alpha,k}$. Carrara

and DesJardin showed that terms conditionally averaged on the phase interface may be directly related to surface averages defined as

$$\left\langle \frac{1}{\rho_\pm} Q_\pm a^I|_{\gamma=0\pm} \right\rangle \equiv \frac{\int_\infty \mathrm{d}^3x' G\xi Q_\pm a^I}{\int_\infty \mathrm{d}^3x' G\rho_\pm \xi} = \frac{\oint_{\partial\Omega_\pm} \mathrm{d}^2x' G Q^I_\pm}{\oint_{\partial\Omega_\pm} \mathrm{d}^2x' G\rho^I_\pm} = \frac{A_\pm}{V_\pm} \frac{\overline{(Q_\pm)_s}}{\overline{(\rho_\pm)_s}}, \tag{7}$$

where $Q_\pm$ is an arbitrary quantity associated with one or the other of two separated phases and A and V are the associated area and volume associated with that phase. This relation is key in interpreting the conditional averages and will be used to develop closure models in Section 3.

For the droplet phase, a similar procedure may be employed to determine the marginal VSFMDF for the liquid phase. For this case, conditionally filtered quantities within the phase are neglected since the properties are assumed to be uniform. The result is a Liouville equation governing the time rate of change of the dispersed phase FMDF where only conditionally surface filtered quantities remain, except for the body force which acts everywhere,

$$\begin{aligned}\frac{\partial F^{\mathrm{p}}_L}{\partial t} + \frac{\partial}{\partial \mathbf{x}}(\mathbf{u}_{\mathrm{p}} F^{\mathrm{p}}_L) = {} & \frac{\partial}{\partial \Psi_{\alpha,\mathrm{p}}} \left[\left\langle \frac{1}{\rho_{\mathrm{p}}} \Gamma_{\alpha,\mathrm{p}} \nabla \psi^I_{\alpha,\mathrm{p}} \cdot \mathbf{e}^I_{n,\mathrm{p}} a^I|_{\gamma=0^+} \right\rangle F^{\mathrm{p}}_L \right] \\ & - \frac{\partial}{\partial \mathbf{u}_{\mathrm{p}}} \left[\left\langle \frac{1}{\rho_{\mathrm{p}}} P^I_{\mathrm{p}} \mathbf{e}^I_{n,\mathrm{p}} a^I|_{\gamma=0^+} \right\rangle F^{\mathrm{p}}_L \right] \\ & + \frac{\partial}{\partial \mathbf{u}_{\mathrm{p}}} \left[\left\langle \frac{1}{\rho_{\mathrm{p}}} \boldsymbol{\tau}^I_{\sim\mathrm{p}} \cdot \mathbf{e}^I_{n,\mathrm{p}} a^I|_{\gamma=0^+} \right\rangle F^{\mathrm{p}}_L \right]. \\ & - \frac{\partial}{\partial \mathbf{u}_{\mathrm{p}}} [\langle \phi_{\mathrm{p}} \mathbf{f}_{\mathrm{p}}|_{\gamma>0^+} \rangle F^{\mathrm{p}}_L]. \end{aligned} \tag{8}$$

The first term on the r.h.s. of the equality in Eq. (8) is the flux of $\psi_{\alpha,\mathrm{p}}$ in the liquid phase at the phase boundary. Physically, this term represents heat or mass transfer from one phase to the other when the dispersed phase temperature or species mass fraction are contained in $\psi_{\alpha,\mathrm{p}}$. The second and third terms on the r.h.s. represent pressure and viscous drag on the particulate due to the presence of the gas phase.

3. Closure of the FDF transport equations

The conditionally filtered quantities in Eqs. (6) and (8) require modeling for the gas and liquid phases, respectively. The following subsections discuss each of these separately including associated terms that require modeling within the phase (*i.e.*, $\gamma < 0^-$ or $\gamma > 0^+$) and on the phase interface ($\gamma = 0^+$ or $\gamma = 0^-$).

3.1. Liquid droplet phase closures

As seen in Eq. (8), closure of phase-averaged properties are required. For the current study, it is assumed that the droplets may be described by a point description for which the following set of conservation equations are applicable: mass, energy and momentum for an individual droplet in the absence of gravity

$$\frac{\mathrm{d}m_{\mathrm{p}}}{\mathrm{d}t} = \dot{m}_{\mathrm{p}} = -\pi d_{\mathrm{p}} \frac{\mu_{\mathrm{g}}}{Sc_{\mathrm{g}}} B_{\mathrm{M}} Sh_{\mathrm{g}}, \tag{9}$$

$$m_{\mathrm{p}} C_{v,\mathrm{p}} \frac{\mathrm{d}T_{\mathrm{p}}}{\mathrm{d}t} = \pi d_{\mathrm{p}} \frac{\mu_{\mathrm{g}} C_{p,\mathrm{g}}}{Pr_{\mathrm{g}}} (T_{\mathrm{g}} - T_{\mathrm{p}}) Nu_{\mathrm{g}} + \dot{m}_{\mathrm{p}} L_{\mathrm{vap}}, \tag{10}$$

$$m_{\mathrm{p}} \frac{\mathrm{d}\mathbf{v}_{\mathrm{p}}}{\mathrm{d}t} = \frac{\pi}{8} \rho_{\mathrm{g}} d^2_{\mathrm{p}} C_D |\mathbf{v}_{\mathrm{g}} - \mathbf{v}_{\mathrm{p}}| (\mathbf{v}_{\mathrm{g}} - \mathbf{v}_{\mathrm{p}}), \tag{11}$$

where d_{p} is the droplet diameter, μ_{g} is the gas-phase molecular viscosity, ρ_{g} is the gas-phase mass density, $C_{p,\mathrm{g}}$ and $C_{v,\mathrm{p}}$ are the gas and droplet phase specific heats and C_D is the coefficient of drag and is approximated for a sphere as: $C_D = 24(1 + Re^{2/3}/6)/Re_{\mathrm{p}}$ for $Re_{\mathrm{p}} < 1000$ and $C_D = 0.424$ for $Re_{\mathrm{p}} \geqslant 1000$ where $Re_{\mathrm{p}} (= \rho_{\mathrm{g}} d_{\mathrm{p}} |\mathbf{v}_{\mathrm{g}} - \mathbf{v}_{\mathrm{p}}|/\mu_{\mathrm{g}})$ is the droplet Reynolds number. Ranz–Marshall correlations are used to determine the Sherwood and Nusselt numbers ($Sh_{\mathrm{g}} = Nu_{\mathrm{g}} = 2[1 + Re^{1/2}_{\mathrm{p}} Sc^{1/3}_{\mathrm{g}}/3] \ln(1 + B_{\mathrm{M}})/B_{\mathrm{M}}$) where $B_{\mathrm{M}} (= (Y_{\mathrm{s}} - Y_{\mathrm{g}})/(Y_{\mathrm{p}} - Y_{\mathrm{s}}))$ is the mass transfer number and a unity Lewis number is assumed (Ranz and Marshall, 1952). Given the description of the droplet field from Eq. (11), the surface conditional averages in Eq. (8) can now be closed using (7) resulting in the following:

$$\begin{aligned}\frac{\partial F^{\mathrm{p}}_L}{\partial t} + \frac{\partial}{\partial \mathbf{x}}(\mathbf{u}_{\mathrm{p}} F^{\mathrm{p}}_L) = {} & \frac{\partial}{\partial T_{\mathrm{p}}} \left[\frac{\pi d_{\mathrm{p}} \mu_{\mathrm{g}} C_{p,\mathrm{g}}}{m_{\mathrm{p}} Pr_{\mathrm{g}} C_{v,\mathrm{p}}} (\widetilde{T}_{\mathrm{g}} - T_{\mathrm{p}}) Nu_{\mathrm{g}} F^{\mathrm{p}}_L \right] \\ & - \frac{\partial}{\partial T_{\mathrm{p}}} \left[\frac{L_{\mathrm{vap}} \pi \mu_{\mathrm{g}} B_{\mathrm{M}} d_{\mathrm{p}} Sh_{\mathrm{g}}}{m_{\mathrm{p}} C_{v,\mathrm{p}} Sc_{\mathrm{g}}} F^{\mathrm{p}}_L \right] \\ & - \frac{\partial}{\partial m_{\mathrm{p}}} \left[\frac{d_{\mathrm{p}} \pi \mu_{\mathrm{g}} B_{\mathrm{M}}}{Sc_{\mathrm{g}}} Sh_{\mathrm{g}} F^{\mathrm{p}}_L \right] \\ & - \frac{\partial}{\partial \mathbf{u}_{\mathrm{p}}} \left[\frac{\pi \rho_{\mathrm{g}} C_D d^2_{\mathrm{p}}}{8 m_{\mathrm{p}}} |\tilde{\mathbf{v}}_{\mathrm{g}} - \mathbf{u}_{\mathrm{p}}| (\tilde{\mathbf{v}}_{\mathrm{g}} - \mathbf{u}_{\mathrm{p}}) F^{\mathrm{p}}_L \right], \end{aligned} \tag{12}$$

where $\tilde{f}_k \equiv \langle \phi_k f_k \rangle / \langle \phi_k \rho_k \rangle = \langle \phi_k f_k \rangle / (\theta_k \overline{\rho}_k)$, consistent with Carrara and DesJardin (2006). As a first step, the gas-phase information in Eq. (12) is expressed in terms of the local filtered properties. More advanced closures could also be constructed using local gas-phase Monte-Carlo particle information using a direct exchange model (Fox, 2003).

3.2. Gas-phase closures

The terms associated with $\gamma < 0^-$ are conditional averages within the gas phase where as a first step it is assumed that closure models for single-phase FDF formulations may be used (Sheikhi et al., 2003; Gicquel et al., 2002; Colucci et al., 1998) under the conditions of low droplet mass loading. With this assumption the generalized Langevin model (GLM) and linear mean square estimation (LMSE) models are employed

$$\frac{\partial^2}{\partial \Psi_{\alpha,\mathrm{g}} \partial \Psi_{\beta,\mathrm{g}}} \left[\left\langle \phi_{\mathrm{g}} \Gamma_{\alpha,\mathrm{g}} \frac{\partial \psi_{\alpha,\mathrm{g}}}{\partial \mathbf{x}} \cdot \frac{\partial \psi_{\beta,\mathrm{g}}}{\partial \mathbf{x}}|_{\gamma<0-} \right\rangle F^{\mathrm{g}}_L \right] \overset{\text{modeled}}{=\!=\!=} \frac{\partial}{\partial \Psi_{\alpha,\mathrm{g}}} [\Omega_m (\Psi_{\alpha,\mathrm{g}} - \tilde{\psi}_{\alpha,\mathrm{g}}) F^{\mathrm{g}}_L] \tag{13}$$

and

$$\frac{\partial}{\partial \mathbf{u}_g}\left[\left\langle \frac{1}{\rho_g}\nabla(\phi_g P_g)|_{\gamma<0-}\right\rangle F_L^g - \frac{1}{\langle\rho_g\rangle}\frac{\partial\langle P_g\rangle}{\partial \mathbf{x}}F_L^g\right] - \frac{\partial^2}{\partial \mathbf{u}_g\cdot\partial\mathbf{u}_g}\left[\left\langle \phi_g\mu_g\frac{\partial \mathbf{v}_g}{\partial \mathbf{x}}\cdot\frac{\partial \mathbf{v}_g}{\partial \mathbf{x}}|_{\gamma<0-}\right\rangle F_L^g\right] - \frac{\partial^2}{\partial \mathbf{u}_g\partial\Psi_{\alpha,g}}\left[\left\langle \phi_g\mu_g\frac{\partial \mathbf{v}_g}{\partial \mathbf{x}}\cdot\frac{\partial\psi_{\alpha,g}}{\partial \mathbf{x}}|_{\gamma<0-}\right\rangle F_L^g\right] - \frac{1}{\langle\rho_g\rangle}\frac{\partial^2}{\partial\Psi_{\alpha,g}\partial\mathbf{u}_g}\left[\left\langle \rho_g\phi_g\Gamma_{\alpha,g}\frac{\partial\psi_{\alpha,g}}{\partial \mathbf{x}}\cdot\frac{\partial \mathbf{v}_g}{\partial \mathbf{x}}|_{\gamma<0}\right\rangle F_L^g\right] \overset{\text{modeled}}{=\!=\!=} \frac{C_o\epsilon}{2}\frac{\partial^2 F_L^g}{\partial \mathbf{u}_g\cdot\partial\mathbf{u}_g} + \nu_g\left(\frac{\partial\tilde{\mathbf{v}}_g}{\partial \mathbf{x}}\cdot\frac{\partial\tilde{\mathbf{v}}_g}{\partial \mathbf{x}}\right)\frac{\partial^2 F_L^g}{\partial \mathbf{u}_g\cdot\partial\mathbf{u}_g} + 2\nu_g\frac{\partial\tilde{\mathbf{v}}_g}{\partial \mathbf{x}}\cdot\frac{\partial^2 F_L^g}{\partial \mathbf{x}\cdot\partial\mathbf{u}_g} - \frac{\partial}{\partial \mathbf{u}_g}[\underset{\sim}{\mathbf{G}}\cdot(\mathbf{u}_g-\tilde{\mathbf{v}}_g)F_L^g], \tag{14}$$

where $\mathbf{G} = -\omega(1/2+2C_o/3)\,\mathbf{I}, \omega = \epsilon/k$ is the turbulent mixing frequency, and $\Omega_m = \tilde{C}_\phi\omega$. The turbulent dissipation and turbulent kinetic energy are given by $\epsilon = C_\epsilon k^{3/2}/\Delta_f$ and $k = 1/2(\widetilde{\mathbf{v}_g\cdot\mathbf{v}_g} - \tilde{\mathbf{v}}_g\cdot\tilde{\mathbf{v}}_g)$, respectively. The dynamic and kinematic viscosities in the gas phase are given by ν_g and μ_g. The parameters C_o, C_ϵ and C_ϕ are modeling constants that must be specified and Δ_f is the LES filter width (Sheikhi et al., 2003). For the simulations conducted here, values suggested in the literature, $C_o = 2.1$, $C_\epsilon = 1$ and $C_\phi = 1$ are adopted (Pope, 1994).

The remaining last three unclosed terms on the r.h.s of Eq. (6) are surface filtered terms conditioned upon $\gamma = 0^-$. The first term conditioned on the interface involves the gradient of the gas-phase conserved quantity $\psi_{\alpha,g}$ representing the fields: $\psi_{\alpha,g} = \{T_g, Y_{\beta,g}\}$ for $\alpha = \{T,\beta\}$ with $\mathbf{J}_{T,g} = -\kappa_g\nabla T_g$ and $\mathbf{J}_{\beta,g} = -\rho_g\mathscr{D}_m\nabla Y_{\beta,g}$ where κ_g is the gas-phase thermal conductivity and $\mathscr{D}_m$ is the gas-phase diffusivity. For the problem considered here: water and air, $\beta = \{\mathrm{Air},\mathrm{H_2O}\}$ represents the relative mass fractions of the species of air and water. These terms are closed in terms of droplet properties using interface matching conditions. In what follows, the interface normal is determined from the interface function, $\gamma(\mathbf{x},t)$, and is taken to be positive oriented outward from the droplets phase with $\mathbf{e}^I_{n,g} = -\mathbf{e}^I_{n,p}$, as shown in Fig. 1.

The interface matching condition for energy, neglecting radiation and chemical reactions at the surface, can be written as (Kataoka, 1986; Carrara and DesJardin, 2006)

$$\sum_{k=1}^{2}\left\{\rho_k^I h_k^I(\mathbf{v}_k-\mathbf{v}^I)\cdot\mathbf{e}^I_{n,k} - \frac{\mu_k}{Sc_k}\nabla h_k^I\cdot\mathbf{e}^I_{n,k} - \underset{\sim}{\boldsymbol{\sigma}}_k\cdot\mathbf{v}_k^I\cdot\mathbf{e}^I_{n,k}\right\} = 0. \tag{15}$$

Disregarding surface tension and substituting in for the mass flux in terms of the quasi-steady droplet model then the heat flux on the gas side of the interface may be explicitly determined

$$-\frac{\mu_g}{Sc_g}\nabla h_g^I\cdot\mathbf{e}_p^I = \dot{m}_g''L_{\mathrm{vap}} - \kappa_p\nabla T_p^I\cdot\mathbf{e}_p^I = \frac{4\pi\kappa_g r_s}{C_{p,g}}\ln(1+B_T)L_{\mathrm{vap}} + \frac{\pi d_p C_{p,g}\mu_g}{Pr_g}(T_\infty - T_p(r_s))Nu, \tag{16}$$

where $\dot{m}_p'' = \dot{m}_g''$ and $L_{\mathrm{vap}} = h_g - h_p$ and a unity Lewis number is assumed. Substituting Eq. (16) into Eq. (6) and using Eq. (7) then results in the following closure for the enthalpy term:

$$\frac{\partial}{\partial h_g}\left[\left\langle\frac{\kappa_g}{\rho_g}\nabla T_g\cdot\mathbf{e}_g^I a^I|_{\gamma=0-}\right\rangle F_L^g\right] = \frac{\partial}{\partial h_g}\left[\frac{A_g}{V_g}\left(\frac{4\pi\kappa_g\tilde{r}}{\tilde{A}_p C_{p,g}}ln(1+B_M)L_{\mathrm{vap}} + \frac{\pi\langle d_p\rangle C_{p,g}\mu_g}{Pr_g}(T_\infty - T_p(r_s))Nu\right)F_L^g\right] = \frac{\partial}{\partial h_g}[S_T F_L^g]. \tag{17}$$

The phase-coupling term involving the species mass fraction for the gas-phase are determined by considering species conservation across the interface for $Y_{\beta,g}$ with $\beta = \{\mathrm{Air},\mathrm{H_2O}\}$

$$\rho_g\mathscr{D}_m\frac{\mathrm{d}Y_{\mathrm{H_2O},g}}{\mathrm{d}r} = \dot{m}_g''(Y_{\mathrm{H_2O},g}-1), \tag{18a}$$

$$\rho_g\mathscr{D}_m\frac{\mathrm{d}Y_{\mathrm{air},g}}{\mathrm{d}r} = \dot{m}_g''(Y_{\mathrm{air},g}-1). \tag{18b}$$

Substituting Eq. (18b) into Eq. (17) yields

$$\frac{\partial}{\partial Y_{\beta,g}}[\langle\mathscr{D}_m\nabla Y_{\beta,g}\cdot\mathbf{e}^I_{n,g}a^I|_{\gamma=0-}\rangle F_L^g] = \frac{\partial}{\partial Y_{\mathrm{Air},g}}\left[\frac{A_g}{V_g}\frac{\pi\tilde{d}_p\mu_g}{\overline{\rho}_g Sc_g}B_M Sh_g(\widetilde{Y}_{\mathrm{air},g}-1)F_L^g\right] + \frac{\partial}{\partial Y_{\mathrm{H_2O},g}}\left[\frac{A_g}{V_g}\frac{\pi\tilde{d}_p\mu_g}{\overline{\rho}_g Sc_g}B_M Sh_g(\widetilde{Y}_{\mathrm{H_2O},g}-1)F_L^g\right] = \frac{\partial}{\partial Y_{\mathrm{Air},g}}[S_{Y,\mathrm{air}}F_L^g] + \frac{\partial}{\partial Y_{\mathrm{H_2O},g}}[S_{Y,\mathrm{H_2O}}F_L^g], \tag{19}$$

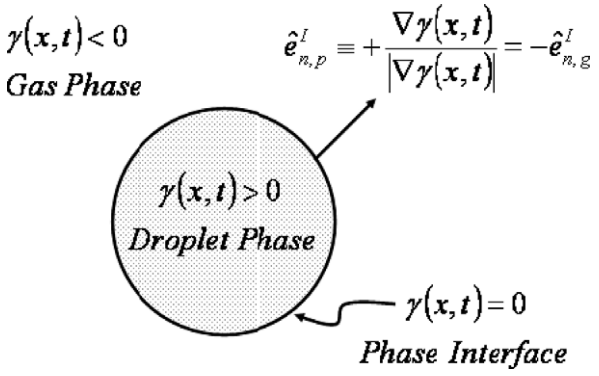

Fig. 1. Orientation of interface unit normal vector.

wherein the filtered density is given as $\overline{\rho}_{\mathrm{g}} = P_o/(R\widetilde{T}_{\mathrm{g}})$ with $R = \mathscr{R}_u/\left(\sum_i \widetilde{Y}_i/MW_i\right)^{-1}$ where $\mathscr{R}_u$ is the universal gas constant and MW_i is the molecular weight for species i.

The last term in the gas-phase TVSFMDF is associated with traction forces on the phase interface. The momentum jump condition across the interface, neglecting surface tension effects can be written as (Kataoka, 1986; Carrara and DesJardin, 2006)

$$\underset{\sim}{\boldsymbol{\sigma}}_{\mathrm{g}} \cdot \mathbf{e}^I_{n,\mathrm{g}} = -\underset{\sim}{\boldsymbol{\sigma}}_{\mathrm{p}} \cdot \mathbf{e}^I_{n,\mathrm{p}} - \dot{m}''_{\mathrm{g}} \mathbf{v}_{\mathrm{g}}. \tag{20}$$

The inner product of the Cauchy stress tensor in the droplet phase with the surface normal is the traction on the droplet surface, $\mathbf{t} = \underset{\sim}{\boldsymbol{\sigma}}_{\mathrm{p}} \cdot \mathbf{e}^I_{n,\mathrm{p}}$. In this context, the surface traction simply represents the drag on the droplet surface by virtue of the gas-phase flow. Employing the particle drag model from Eqs. (11), (20) becomes,

$$\begin{aligned}
&\frac{\partial}{\partial \mathbf{u}_{\mathrm{g}}}\left[\langle \underset{\sim}{\boldsymbol{\sigma}}_{\mathrm{g}} \cdot \mathbf{e}^I_{n,\mathrm{g}} a^I|_{\gamma=0-}\rangle F^{\mathrm{g}}_L\right] \\
&\quad = -\frac{\partial}{\partial \mathbf{u}_{\mathrm{g}}}\left[\frac{A_{\mathrm{g}}}{V_{\mathrm{g}}}\frac{1}{2}\tilde{A}_{\mathrm{p}}\rho_{\mathrm{g}} C_D |\mathbf{u}_{\mathrm{g}} - \langle \mathbf{v}_{\mathrm{p}}\rangle|(\mathbf{u}_{\mathrm{g}} - \tilde{\mathbf{v}}_{\mathrm{p}})F^{\mathrm{g}}_L\right] \\
&\qquad - \frac{\partial}{\partial \mathbf{u}_{\mathrm{g}}}\left[\frac{A_{\mathrm{g}}}{V_{\mathrm{g}}}\frac{4\pi\kappa_{\mathrm{g}}\tilde{r}}{C_{p,\mathrm{g}}\tilde{A}_{\mathrm{p}}}\ln(1+B_{\mathrm{M}})\tilde{\mathbf{v}}_{\mathrm{p}}F^{\mathrm{g}}_L\right] = \frac{\partial}{\partial \mathbf{u}_{\mathrm{g}}}[\mathbf{S}_U F^{\mathrm{g}}_L].
\end{aligned} \tag{21}$$

In Eqs. (17), (19) and (21) the ratio of the surface area to volume, $A_{\mathrm{g}}/V_{\mathrm{g}}$, appears as a pre-multiplication factor. Using the definition of the volume fraction, this term may be expressed in terms of the local particle loading that is determined from the particle Monte-Carlo field

$$\frac{A_{\mathrm{g}}}{V_{\mathrm{g}}} = \frac{A_{\mathrm{g}}}{V_T}\frac{1}{\theta_{\mathrm{g}}} = \frac{4\pi\widetilde{r^2}N_{\mathrm{p}}}{\theta_{\mathrm{g}}\Delta_{\mathrm{f}}^3}. \tag{22}$$

where Δ_{f}^3 is the LES filter volume.

Substituting Eqs. (17), (19), (21) and (22) into Eq. (6) results in the final form of the modeled gas-phase marginal VSFMDF transport equation

$$\begin{aligned}
\frac{\partial F^{\mathrm{g}}_L}{\partial t} + \frac{\partial}{\partial \mathbf{x}}(\mathbf{u}_{\mathrm{g}}F^{\mathrm{g}}_L) &= \frac{\partial}{\partial \mathbf{x}}\left[\nu_{\mathrm{g}}\frac{\partial F^{\mathrm{g}}_L}{\partial \mathbf{x}}\right] + \frac{\partial}{\partial \mathbf{u}_{\mathrm{g}}}\left[\frac{1}{\overline{\rho}_{\mathrm{g}}}\frac{\partial \overline{P}_{\mathrm{g}}}{\partial \mathbf{x}}F^{\mathrm{g}}_L\right] \\
&\quad + \frac{1}{2}C_o\epsilon\frac{\partial^2 F^{\mathrm{g}}_L}{\partial \mathbf{u}_{\mathrm{g}}\cdot\partial \mathbf{u}_{\mathrm{g}}} + \nu_{\mathrm{g}}\left[\frac{\partial \tilde{\mathbf{v}}_{\mathrm{g}}}{\partial \mathbf{x}}\cdot\frac{\partial \tilde{\mathbf{v}}_{\mathrm{g}}}{\partial \mathbf{x}}\right]\frac{\partial^2 F^{\mathrm{g}}_L}{\partial \mathbf{u}_{\mathrm{g}}\cdot\partial \mathbf{u}_{\mathrm{g}}} \\
&\quad + 2\nu_{\mathrm{g}}\frac{\partial \tilde{\mathbf{v}}_{\mathrm{g}}}{\partial \mathbf{x}}\cdot\frac{\partial^2 F^{\mathrm{g}}_L}{\partial \mathbf{x}\cdot\partial \mathbf{u}_{\mathrm{g}}} - \frac{\partial}{\partial \mathbf{u}_{\mathrm{g}}}[\Omega_m(\mathbf{u}_{\mathrm{g}} - \tilde{\mathbf{v}}_{\mathrm{g}})F^{\mathrm{g}}_L] \\
&\quad + \frac{\partial}{\partial T_{\mathrm{g}}}[\Omega_m(T_{\mathrm{g}} - \widetilde{T}_{\mathrm{g}})F^{\mathrm{g}}_L] \\
&\quad + \frac{\partial}{\partial Y_{\mathrm{air,g}}}[\Omega_m(Y_{\mathrm{air,g}} - \widetilde{Y}_{\mathrm{air,g}})F^{\mathrm{g}}_L] \\
&\quad + \frac{\partial}{\partial T_{\mathrm{g}}}[S_T F^{\mathrm{g}}_L] + \frac{\partial}{\partial Y_{\mathrm{air,g}}}[S_{Y,\mathrm{air}}F^{\mathrm{g}}_L] \\
&\quad + \frac{\partial}{\partial Y_{\mathrm{H_2O,g}}}[S_{Y,\mathrm{H_2O}}F^{\mathrm{g}}_L] + \frac{\partial}{\partial \mathbf{u}_{\mathrm{g}}}[\mathbf{S}_U F^{\mathrm{g}}_L].
\end{aligned} \tag{23}$$

4. Statistically equivalent stochastic differential equations

Eqs. (12) and (23) comprise a system of two Fokker–Planck equations (FPE) for the two-phase flow. The approach used to solve these equations employs the so called "principle of equivalent systems" (Pope, 1985) which allows for the determination of a system of statistically equivalent stochastic differential equations (SDE) that are solved in lieu of the original FPE.

4.1. Droplet phase ODEs

Using the principle of equivalent systems, the system of differential equations corresponding to Eq. (12) is

$$\mathrm{d}\mathbf{X}^+_{\mathrm{p}} = \mathbf{U}^+_{\mathrm{p}}\,\mathrm{d}t, \tag{24a}$$

$$\mathrm{d}\mathbf{U}^+_{\mathrm{p}} = \frac{\pi\rho_{\mathrm{g}}C_D d_{\mathrm{p}}^2}{8M^+_{\mathrm{p}}}|\tilde{\mathbf{v}}_{\mathrm{g}} - \mathbf{U}^+_{\mathrm{p}}|(\tilde{\mathbf{v}}_{\mathrm{g}} - \mathbf{U}^+_{\mathrm{p}})\mathrm{d}t, \tag{24b}$$

$$\mathrm{d}T^+_{\mathrm{p}} = \frac{\pi d_{\mathrm{p}}\mu_{\mathrm{g}}C_{p,\mathrm{g}}}{M^+_{\mathrm{p}}Pr_{\mathrm{g}}C_{v,p}}(\widetilde{T}_{\mathrm{g}} - T^+_{\mathrm{p}})Nu_{\mathrm{g}}\,\mathrm{d}t - \frac{L_{\mathrm{vap}}\pi\mu_{\mathrm{g}}B_{\mathrm{M}}d_{\mathrm{p}}Sh_{\mathrm{g}}}{M^+_{\mathrm{p}}C_{v,p}Sc_{\mathrm{g}}}\mathrm{d}t, \tag{24c}$$

$$\mathrm{d}M^+_{\mathrm{p}} = -\frac{d_{\mathrm{p}}\pi\mu_{\mathrm{g}}B_{\mathrm{M}}}{Sc_{\mathrm{g}}}Sh_{\mathrm{g}}\,\mathrm{d}t, \tag{24d}$$

where the superscript "+" is used to denote the notional Monte-Carlo particle for the corresponding physical variable and accounts for compositional changes in droplet location, velocity, temperature and mass. These equations are directly coupled to the gas-phase through their dependence on the temperature and velocity in Eqs. (24b) and (24c), respectively, and indirectly through Re, Sh, Nu, and C_D. It is of importance to note that because the velocity is included in the phase-space in the VSFDF formulation, the convection is in closed form and therefore the filtered velocity fluctuation does not appear in the above equations. Consequently, only the phase-averaged gas-phase velocity, $\tilde{\mathbf{v}}_{\mathrm{g}}$ and the instantaneous droplet phase Monte-Carlo velocity, $\mathbf{U}^+_{\mathrm{p}}$ are included.

4.2. Gas-phase SDEs

The equivalent stochastic differential equations (SDEs) for the gas-phase system are in general non-unique, however, guidance on the construction of the SDEs may be found in Sheikhi et al. (2003) resulting in the following:

$$\mathrm{d}\mathbf{X}^+_{\mathrm{g}} = \mathbf{U}^+_{\mathrm{g}}\,\mathrm{d}t + \sqrt{2\nu_{\mathrm{g}}}\,\mathrm{d}\mathbf{W}^X, \tag{25a}$$

$$\begin{aligned}
\mathrm{d}\mathbf{U}^+_{\mathrm{g}} &= [\nabla\overline{P}_{\mathrm{g}} + 2\nu_{\mathrm{g}}\nabla^2\tilde{\mathbf{v}}_{\mathrm{g}} + \underset{\sim}{\mathbf{G}}\cdot(\mathbf{U}^+_{\mathrm{g}} - \tilde{\mathbf{v}}_{\mathrm{g}})]\mathrm{d}t \\
&\quad + \sqrt{2\nu_{\mathrm{g}}}\nabla\otimes\tilde{\mathbf{v}}_{\mathrm{g}}\cdot\mathrm{d}\mathbf{W}^X + \sqrt{C_o\epsilon}\,\mathrm{d}\mathbf{W}^U + \mathbf{S}_U\,\mathrm{d}t,
\end{aligned} \tag{25b}$$

$$\mathrm{d}T^+_{\mathrm{g}} = -C_\phi\Omega_m(T^+_{\mathrm{g}} - \widetilde{T}_{\mathrm{g}})\mathrm{d}t + S_T\,\mathrm{d}t, \tag{25c}$$

$$\mathrm{d}Y^+_{\mathrm{air,g}} = -C_\phi\Omega_m(Y^+_{\mathrm{air,g}} - \widetilde{Y}_{\mathrm{air,g}})\mathrm{d}t + S_{Y,\mathrm{air}}\,\mathrm{d}t, \tag{25d}$$

where $\mathbf{W}^X$ and $\mathbf{W}^U$ denote statistically independent Wiener–Lèvy stochastic processes (Gardiner, 1982). The effects of the liquid phase appears in these equations through the source terms, $\mathbf{S}_U, S_T$ and $S_{Y,\text{air}}$ and the volume fraction.

Eqs. (24b)–(24d) and (25b)–(25d) comprise a system of non-linear ODEs and SDEs which are solved simultaneously using Monte-Carlo methods. The details of the numerical procedure to solve these equations are discussed next.

5. Numerical solution procedure

The marginal TVSMFDF for each phase is represented as an ensemble of N_p statistically identical Monte-Carlo (MC) particles. Each particle is transported in physical and composition space according to their respective SDE/ODEs. The general solution approach is based on the use of a stand-alone full particle based implementation for both phases of the flow. The method is a combination of a "grid free" Lagrangian approach for the notional particle time evolution with a computational grid for estimating mean fields and solving a corrected pressure Poisson equation to drive the flow. A fractional step methodology is implemented when integrating the SDEs ensuring that the solenoidal character of the field in the incompressible (low Mach number) formulation is enforced based on the approach of Minier and Pozorski (1999) and Minier and Peirano (2001). A flow diagram of the overall algorithm is summarized in Fig. 2.

5.1. Numerical solution procedure: gas-phase SDEs

Some care must be taken when integrating the system of stochastic differential equations in the gas phase. General predictor–corrector algorithms cannot be implemented for temporal integration of the SDEs without violating Itô calculus: the "predictor" step extrapolates an intermediate value of the integrated quantity at a future time, $t + \Delta t$. When integrating the SDE's, the Markovian character of the diffusion process must be preserved, and because the future probabilities associated with the Markov processes are determined from its most recent values, this extrapolation is not acceptable (Gardiner, 1982). Therefore, a modified Euler–Maruyamma approximation is implemented for temporal integration that preserves the Itô–Gikhman nature of the SDEs (Cao and Pope, 2003; Gardiner, 1982). Given the Itô SDE:

$$\mathrm{d}\mathbf{X}^{+(n)} = \mathbf{A}^{(n)}(\mathbf{X}^{+(n)}[t], t)\mathrm{d}t + \underset{\sim}{\mathbf{B}}^{(\mathbf{n})}(\mathbf{X}^{+(n)}[t], t) \cdot \mathrm{d}\mathbf{W}^n(t), \quad (26)$$

the finite difference approximation is given by

$$\mathbf{X}^{+(n)1/2} \equiv \mathbf{X}^{+(n)}(t) + \frac{\Delta t}{2}\mathbf{A}^{(n)}(\mathbf{X}^{+(n)}[t], t), \quad (27)$$

$$\mathbf{X}^{+(n)1/2}(t+\Delta t) = \mathbf{X}^{+(n)}(t) + \Delta t\mathbf{A}^{(n)}(\mathbf{X}^{+(n)1/2}, t+\Delta t) + B^{(n)}(\mathbf{X}^{+(n)}, t+\Delta t)\sqrt{\Delta t}\zeta^{(n)}(t), \quad (28)$$

where $\zeta^{(n)}(t)$ is a Gaussian distributed random variable. The above scheme exhibits strong convergence of order 1/2 and weak convergence of order 1 (Xu and Pope, 1999). The intermediate step $\mathbf{X}^{+1/2}$ is a second-order accurate midpoint scheme, and when the diffusion step is added, the entire scheme is weak first-order accurate (Cao and Pope, 2003). The drift and diffusion coefficients, $\mathbf{A}$ and $\mathbf{B}$ specified by Eqs. (25b)–(25d), require mean-field information from the gas phase and mean-field information from the droplet phase in the phase-coupling terms. Mean fields are obtained from the particle properties in both phases *via* a non-parametric kernel estimation method based on linear spline basis functions that is analogous to a "cloud-in-cell" procedure (Dreeben and Pope, 1992). The general solution approach is based on the use of a stand-alone full particle based implementation for both phases of the flow. As noted, a fractional step methodology is implemented when integrating the SDEs ensuring that the solenoidal character of the field in the incompressible (low Mach number) formulation is enforced and consequently a corrected pressure gradient is obtained. The implementation is similar to the full particle approaches of Anand et al. (1997), Delarue and Pope (1998) and Minier and Pozorski (1995, 1999). The interested reader is directed to the excellent article by Minier and Pozorski (1999) wherein a detailed schematic of a pressure-correction fractional step method, developed by Minier and Pozorski, is implemented with great success for the simulation of turbulent channel flow. The computational time step is calculated dynamically so that the integration time step for a given MC particle in both phases (although this is only the "overall" step in the droplet phase, where sub-cycling is used) is limited to the smallest value: $\min\{\mathrm{d}t_\text{g}, \mathrm{d}t_\text{p}\}$, where

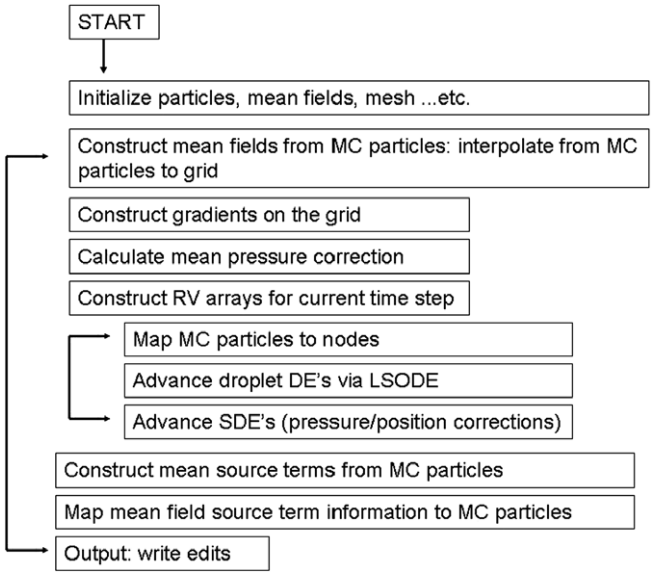

Fig. 2. Flow diagram of particle algorithm.

$$dt_g = \frac{1}{10}\frac{dx}{\sqrt{U^2_{g,max} + V^2_{g,max}}}, \quad (29)$$

$$dt_p = \frac{1}{10}\frac{dx}{\sqrt{U^2_{p,max} + V^2_{p,max}}}. \quad (30)$$

With $|\mathbf{U}^+_{k,max}| = \sqrt{\left(\left(\mathrm{U}^+_{k,max}\cdot \mathrm{e}_1\right)^2 + \left(\mathrm{U}^+_{k,max}\cdot \mathrm{e}_2\right)^2\right)}$ where $\mathbf{U}^+_{k,max} \equiv U^+_{k,max}\mathbf{e}_1 + V^+_{k,max}\mathbf{e}_2$ is the maximum velocity for any given MC particle in each phase at time t with $k = \{p, g\}$ and the subscripts 1 and 2 denoting the directions x and y, respectively. In this implementation the uniform computational mesh spacing is given by dx. The time step is chosen in this way so that it take any given MC particle at least 10 iterations to entirely cross a computational cell.

Information is interpolated to the particle field from the mean field, and *vice versa*, using a weighted bilinear CIC interpolation routine. Other higher-order interpolation schemes have been attempted with varying degrees of success in single-phase FDF simulations (Colucci et al., 1998) and CIC approach is pursued here because in the two-phase simulation, a relatively accurate and computationally efficient interpolation method is necessary. This is particularly true here as where a large number of MC particles are needed to minimize statistical error in the gas phase using the full "stand-alone" solution approach. In hybrid LES velocity-scalar FDF methods for single-phase flow, it is found that approximately 40 particles per cell is acceptable for some flows (Sheikhi et al., 2003), herein more than 25 times this amount are used to reduce the statistical noise to sufficiently low levels.

5.2. Numerical solution procedure: droplet phase ODEs

In the solution procedure, the droplet phase equations are integrated in-step with the SDE's in the gas phase. The droplet phase equations comprise a set of coupled non-linear ordinary differential equations that require numerical integration techniques suitable for a numerically stiff system of ODE's. The droplet equations are integrated in a fractional step methodology using the LSODE (Lawrence Livermore Solver for Ordinary Differential Equations) library (Radhakrishnan and Hindmarsh, 1993). First the gas-phase equations are advanced one time step at which time mean-field information needed in the droplet phase DE's is obtained from the gas-phase particle field. The droplet equations are subsequently integrated with a local time step, calculated from the gas-phase advancement, with transient sub-cycling until convergence criterion is met.

6. Problem setup

The flow geometry of interest is that of a temporally developing counter-current mixing layer, shown schematically in Fig. 3. The temporally developing mixing layer

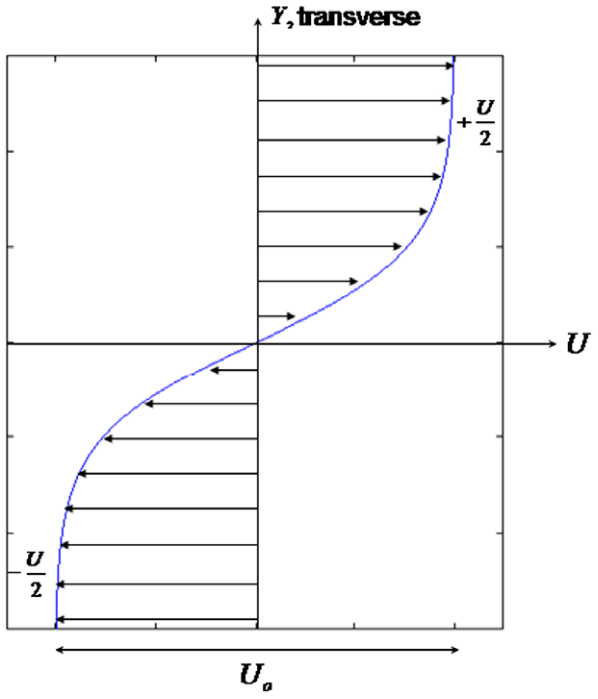

Fig. 3. Sketch of the base gas flow. Note: the mean velocity profile curvature is exaggerated.

consists of two parallel streams traveling in opposite directions with the same speed, U_∞, so that the velocity difference across the layer is $\Delta U = 2U_\infty$. In the temporally developing mixing layer reference frame, the computational domain translates with the mean convective velocity of the primary stream-wise vortices that grow in time. The stream-wise (x) and cross-stream (y) domain lengths are equal with lengths x_{max} and y_{max}, respectively. Periodic boundary conditions are employed at the stream-wise boundaries ($x = 0, x = x_{max}$) and a free-slip boundary condition is applied at the cross-stream boundaries ($y = 0$, $y = y_{max}$).

For the periodic boundary condition, any Monte-Carlo particle leaving the domain at $x = x_{max}$ is mapped *via* a periodic cell to the opposing boundary, and *vice versa*. For the free-slip boundary condition, any Monte-Carlo particles passing through the boundaries $y = 0$ and $y = y_{max}$ are reflected across the boundary with $V^+_p = -V^+_p$, where stream-wise velocity component, U^+_p, and all scalar values are left unchanged. Both the filtered stream-wise velocity and scalar fields are initialized *via* a hyperbolic tangent profile with $\tilde{u}_g = U_\infty, \widetilde{T}_g = T_{hot}$ in the top stream and $\tilde{u}_g = -U_\infty, \widetilde{T}_g = T_{cold}$ in the bottom stream. The species mass fractions are $\widetilde{Y}_{air,g} = 1, \widetilde{Y}_{H_2O,g} = 0$ everywhere for the water droplet laden two-phase flow simulations. The domain length, x_{max} is related to the instability length scale L through the initial vorticity thickness, $\delta_{\Omega,o}(= \Delta U/|\partial U_{g,o}/\partial y|_{max})$, with $U_{g,o}$ the time averaged stream-wise velocity, *via*: $L = x_{max}/\delta_{\Omega,o} = 2^{N_{pair}}\left(\frac{2\pi}{\alpha_{uns}}\right)$ where the most unstable mode, $\alpha_{uns} = 0.4446$, is obtained from a linear

stability analysis of the hyperbolic tangent profile (Michalke, 1964). The formation of large-scale roller structures is facilitated by introducing small harmonic, phase-shifted disturbances containing sub-harmonics of the most unstable mode, determined from a linear stability analysis into the cross-stream and stream-wise initial velocity profiles (Drazin and Reid, 1981; Jackson and Grosch, 1989). One vortical structure is obtained by specifying the number of vortex pairs, $N_{\text{pair}} = 1$ in the definition of the instability length scale, L.

For gas phase analysis, physical parameters in the gas phase are given as $x_{\max} = 0.1$ m, $T_{\text{hot}} = 360$ K, $T_{\text{cold}} = 300$ K, with air being the working fluid with $Re_{\Omega} = 2\Delta U \delta_{\Omega,o}/\nu_{\text{air}} = 25$ where $\delta_{\Omega,o} = 0.002095$ m and $t_{\max} = 6$ s. Simulations are conducted on equally spaced grid points with $\mathrm{d}x = \mathrm{d}y$. All FMDF simulations are conducted on a 51×51 computational grid. The gas-phase Monte-Carlo particles are initially uniformly distributed over the computational domain with 1464 particles per cell. The large number of Monte-Carlo particles is necessary to reduce noise in the full particle based computational method. The computational time is increased with the large number of MC particles, but not restrictively so; simulation times varied from 20 to 30 h depending on the interpolation scheme used. Simulations with far less particles, $\approx$ 100–200 per cell dramatically decrease the computational cost (3–4 h) but the results were extremely noisy, and not included here.

7. Gas-phase analysis

Before the two-phase simulation is conducted it is important to ensure that the VSFMDF simulation predicts reasonable gas-phase physics. This is accomplished by comparison of the FMDF results for (1) transient evolution of the momentum thickness, vorticity thickness and total kinetic energy of the gas-phase flow with traditional DNS and LES simulations under the same flow configurations, and (2) SGS momentum information with traditional LES and a hybrid LES-FDF from Drozda (2002) and Sheikhi et al. (2003). The DNS solver used is based on a finite volume formulation with AUSM+ flux vector splitting and standard 4-stage Runge–Kutta time integration. Ninth-order upwind biased stencils are used to construct the convective fluxes at the control volume surfaces. The same descritization is employed for LES which incorporates a dynamic Smagorinsky model for SGS closure. Further details on the DNS/LES code may be found in DesJardin et al. (2004).

An overall measure of the evolution of the gross dynamics of the gas-phase flow may be obtained from the time evolution of the total flow kinetic energy, momentum, and vorticity thicknesses. The total kinetic energy of the flow is calculated directly from the particle field in the FMDF simulation using

$$k_{\text{tot}}(t) = \frac{1}{2}\sum_{n=1}^{N_{\text{p}}}[(U_{\text{g}}^{+}(n))^2 + (V_{\text{g}}^{+}(n))^2]. \tag{31}$$

In the DNS and LES simulations, the total kinetic energy is given by

$$k_{\text{tot}}(t) = \frac{1}{2}\sum_{i=1}^{N_x}\sum_{j=1}^{N_y}[(u_{i,j})^2 + (v_{i,j})^2], \tag{32}$$

where N_x and N_y are the number of computational nodes in the x and y directions and u and v are the components of the resolved and filtered gas-phase velocity for the DNS and LES, respectively.

DNS simulations are conducted on grids of resolution $50 \times 50, 100 \times 100, 200 \times 200, 300 \times 300$ and 500×500 for total kinetic energy, momentum thickness (δ_m) and vorticity thickness (δ_ω) as functions of time.

Fig. 4 shows the transient evolution of the normalized flow field kinetic energy, momentum and vorticity thickness. The total kinetic energy decreases as a function of time because of viscous dissipation, as expected. The DNS is grid independent at grid resolutions of 300×300 and above.

Fig. 5 shows that the transient evolution of the total flow kinetic energy is over-predicted by the LES-DSMAG by almost a constant value of approximately 1%. The VSFMDF simulation also over predicts the value of the kinetic energy, but the amount of over prediction is not constant with time. Predicted values of the total kinetic energy from the VSFMDF simulation fall between that predicted by the DNS and LES-DSMAG simulations, never varying more than about 1% from the DNS. Fig. 6 shows the temporal evolution of the normalized momentum thickness for the DNS, LES-DSMAG and VSFMDF simulations. The LES-DSMAG slightly over predicts the transient growth rate of the momentum thickness, but flow field dynamics are accurately captured. The VSFMDF simulation initially matches both the DNS and LES-DSMAG results well, but under predicts the temporal evolution of the momentum thickness at later times. The largest value of the under prediction is on the order of 8.5% of the maximum. Aside from the under prediction the field dynamics are still captured as evidenced by the overall curvature trend of the momentum thickness curve when compared to the DNS.

The temporal evolution of the normalized vorticity thickness for DNS, LES-DSMAG and VSFMDF simulations is shown in Fig. 7. The vorticity thickness is a differentiated quantity, as opposed to an integrated quantity like the momentum thickness, and an exact match with LES-DSMAG and VSFMDF to the DNS result is difficult. In Fig. 7, the LES-DSMAG simulation initially under predicts the vorticity thickness growth rate and slightly over predicts at later times. The inherently noisy character of the full particle Monte-Carlo method is evident in the calculation of the vorticity thickness. The short time evolution of the vorticity thickness is quite close the DNS, but some variation is observed later in the simulation. The maximum over prediction of the vorticity thickness is approximately 12% from the DNS value, however, the maximum value

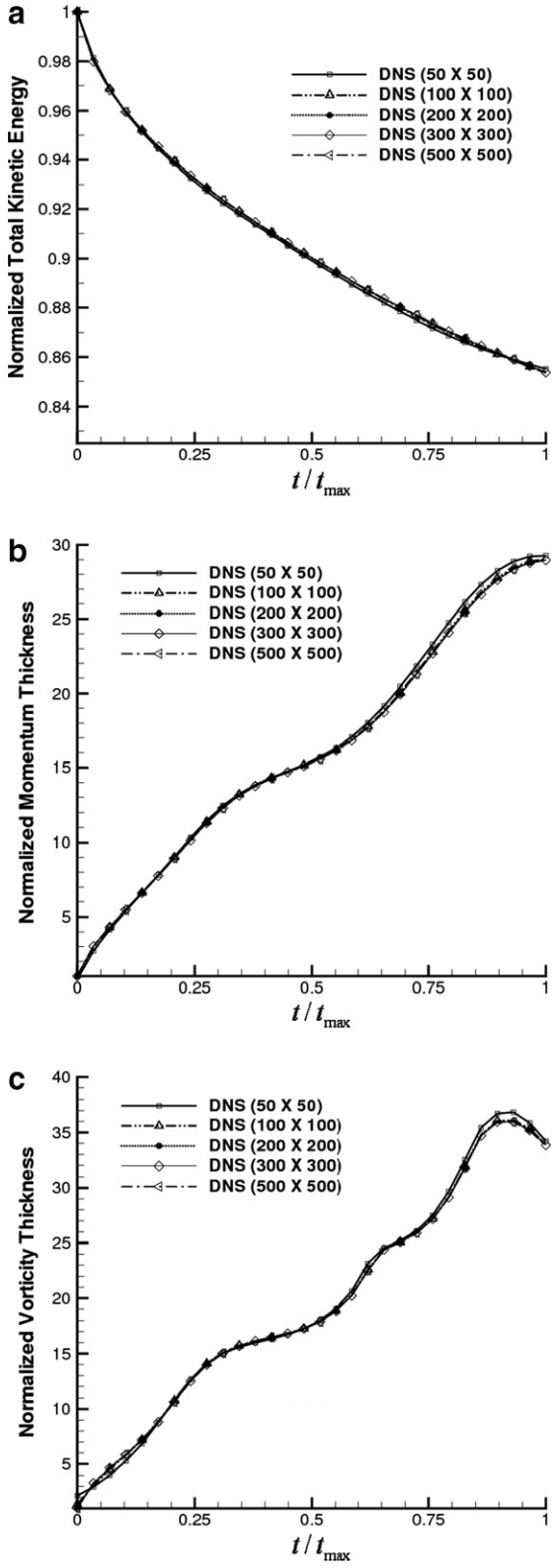

Fig. 4. Temporal evolution of (a) total flow field kinetic energy normalized by its initial value, (b) momentum thickness normalized by its initial value and (c) vorticity thickness normalized by its initial value, all calculated with DNS.

of the vorticity thickness from the VSFMDF simulation under predicts the DNS value by only about 4%.

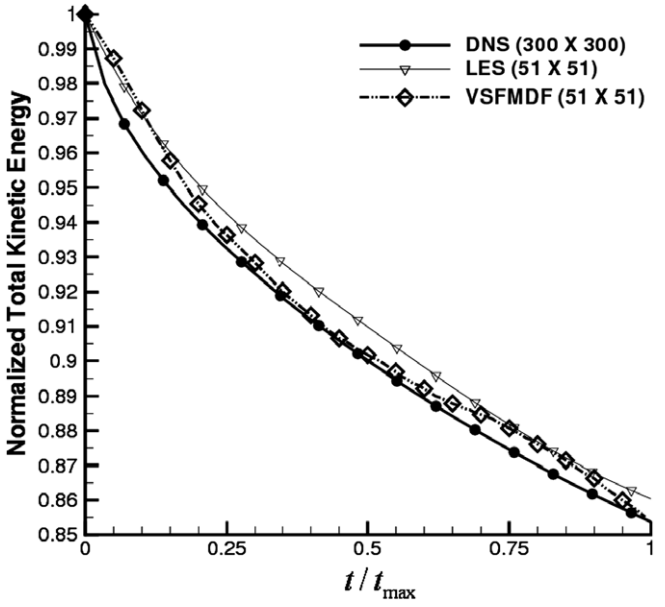

Fig. 5. Temporal evolution of the total flow field kinetic energy normalized by its initial value calculated with DNS, LES-DSMAG and VSFMDF.

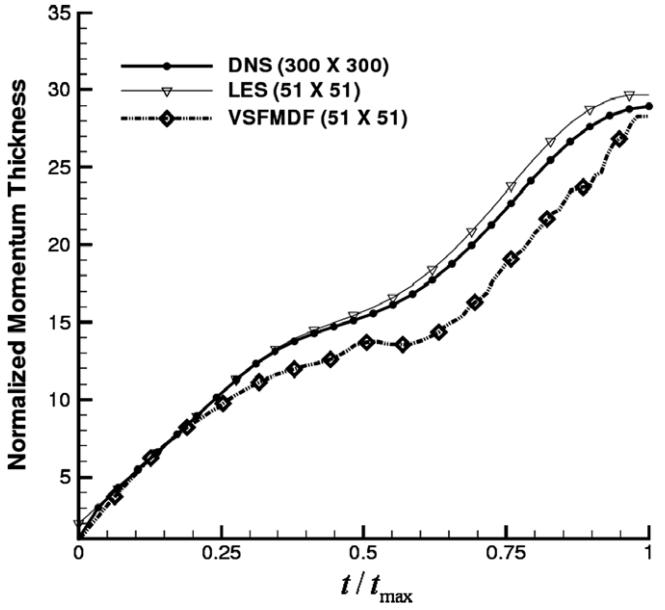

Fig. 6. Temporal evolution of the momentum thickness normalized by its initial value calculated with DNS, LES-DSMAG and VSFMDF.

Fig. 8 shows the statistical variability in the second-order SGS moments where Reynolds averaged values of the correlations, $\langle uu\rangle, \langle uv\rangle$ and $\langle vv\rangle$, with $\tau(a,b) \equiv \langle ab\rangle - \langle a\rangle\langle b\rangle$ (not too be confused with the LES conditional averages), from the VSFMDF simulation are compared to LES-SMAG and LES-FDF simulations of Sheikhi et al. (2003) and Drozda (2002). The SGS correlations are closed *via* a non-dynamic Smagorinsky model (Smagorinsky, 1963; Rogallo and Moin, 1984) where the accuracy and relative advantages and disadvantaged of

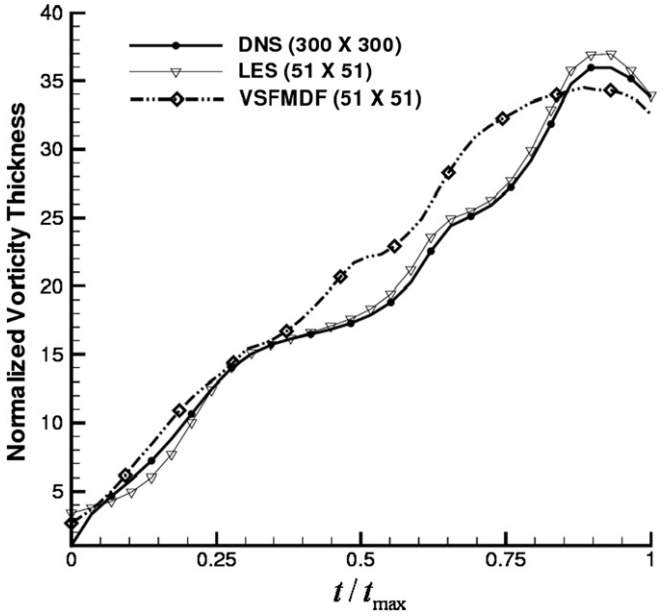

Fig. 7. Temporal evolution of the vorticity thickness normalized by its initial value calculated with DNS, LES-DSMAG and VSFMDF.

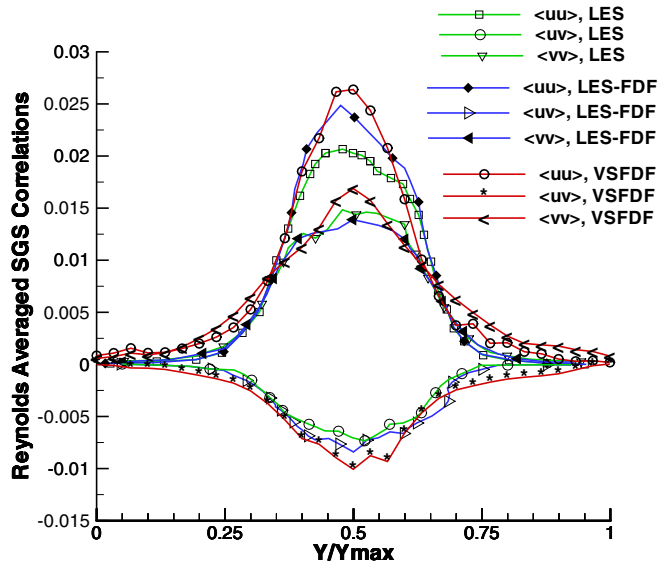

Fig. 8. Cross-stream variation of Reynolds averaged SGS moments calculated with LES-SMAG and LES-FDF of Sheikhi et al. (2003) and Drozda (2002) and VSFMDF from this study.

the SGS model are well-established. In the LES-FDF results, a hybrid method where mean-field information is obtained from a "traditional" LES-SMAG while SGS information is modeled according the velocity-scalar FDF approach was used (Sheikhi et al., 2003). It can be seen that the LES-FDF method slightly over predicts the SGS correlations as compared to the traditional LES-SMAG simulations and the VSFMDF method in turn slightly over predicts the LES-FDF results. For the $\langle uu\rangle$, $\langle uv\rangle$ and $\langle vv\rangle$ correlations, the VSFMDF over predicts the values predicted by the LES-SMAG simulations by approximately 13%, 20% and 15%, respectively. This is in part an artifact of the LMSE closure (Gicquel et al., 2002).

8. Droplet laden flow

For the water droplet laden two-phase flow simulations, the gas-phase velocity is $U_\infty = 1.0\,\mathrm{m/s}$ with $\Delta U = 2\,\mathrm{m/s}$ and $Re_\Omega = 2\Delta U\delta_{\Omega,o}/\nu_{\mathrm{air}} = 188$. The characteristic time scale for droplet/gas simulations, t_c^{drops}, is scaled by the momentum response time $\tau_M(=[\rho_p d_p^2]/[18\mu_g] = StL_{\mathrm{ref}}/u_\infty)$ so that $t_c^{\mathrm{drops}} = t/\tau_M$ with $t_{c,\max}^{\mathrm{drops}} \equiv t_{\max} = 20$. This scaling is chosen so that the droplet relaxation time scale is comparable to the evaporation time scale. Other simulation parameters related to domain length and grid size are identical to the single-phase gas flow: $x_{\max} = 0.1\,m$, grid point in $\mathrm{d}x = \mathrm{d}y$ are equally spaced with a 51×51 computational grid. The gas-phase Monte-Carlo particles are initially uniformly distributed over the computational domain with 1464 particles per cell. There are 2928 droplet phase Monte-Carlo particles uniformly distributed in the lower portion of the flow domain initially at rest and in thermodynamic equilibrium with the gas that is at 300 K and 1 atm. Because the droplets are initially at rest, any movement comes directly from the gas-phase momentum coupling. As the gas flow evolves in time, droplets are swept into the gas-phase roller structure.

Fig. 9 shows representative results for the transient evolution of the droplet phase temperature and number density at times of (a) 0.125 s, (b) 0.25 s, (c) 0.375 s, (d) 0.5 s, (e) 0.625 s and (f) 0.75 s. For this case a 815 μm diameter droplet with an initial Stokes number, $St(=\rho_p d_p^2 u_\infty/18\nu_g x_{\max})$ of 2 is two-way coupled to the gas-phase flow. As the droplets are entrained into the gas phase they are heated *via* and evaporate. The droplets are depleted from the core area of the large-scale roller structure and accumulate in regions of high strain and low vorticity, as is evident by high values of number density in these regions. This observation is consistent with Wen's "stretching" hypothesis (Wen et al., 1992) and DNS simulations of particle laden mixing layers (Wei Ling et al., 1998; Miller and Bellan, 1999; Chein and Chung, 1988) and consistent with the findings of Squires and Eaton (1990) for the dispersion of particles in homogeneous turbulence.

Fig. 10 shows the dispersion, $D(t)$, vs. time for one-way coupled non-evaporating 100 μm,600 μm, and 3800 μm diameter droplets corresponding to St of 0.01, 1 and 50, respectively. The dispersion is defined as

$$D(t) = \sum_{n=1}^{N_p}[(X_p^{n+}(t+\Delta t) - X_p^{n+}(t))^2 + (Y_p^{n+}(t+\Delta t) - Y_p^{n+}(t))^2]/N_p, \tag{33}$$

which provides a measure of the inertial effects on the dispersion for droplets of different mass as a function of time. Droplets with unity Stokes number disperse at a greater rate than either smaller or larger droplets. Similar observations

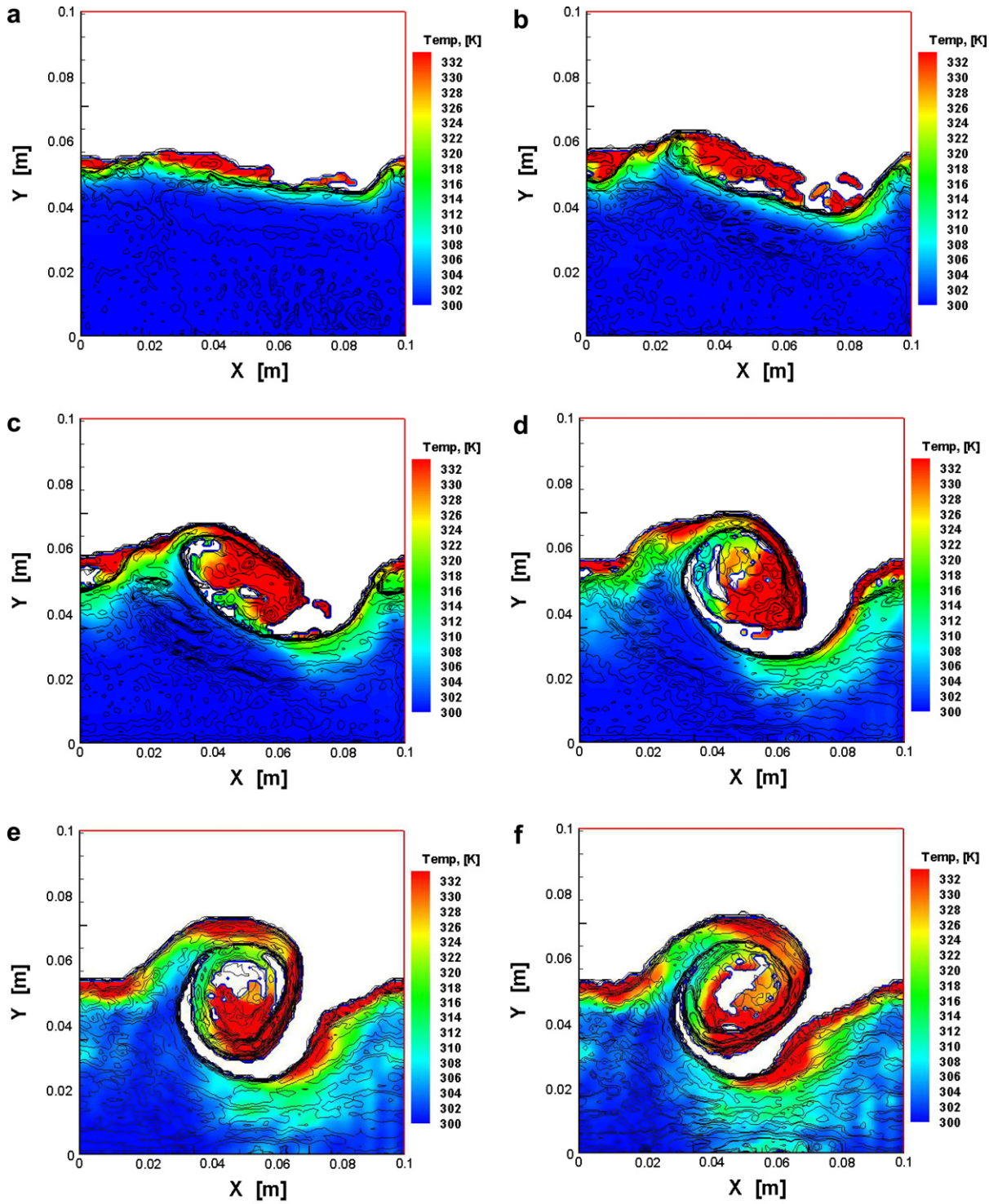

Fig. 9. Droplet temperature contour with droplet number density isolines at (a) $t = 0.125$ s, (b) $t = 0.25$ s, (c) $t = 0.375$ s, (d) $t = 0.5$ s, (e) $t = 0.625$ s, (f) $t = 0.75$ s.

have been noted experimentally where it has been found that turbulent transport of particles can increase as particle size increases in several turbulent flow configurations (Goldschmidt and Eskinazi, 1966; Goldschmidt et al., 1972; Lilly, 1973; Memmot and Smoot, 1978; Yuu et al., 1978). This result has also been noted in DNS simulations of particle laden turbulent flows (Chein and Chung, 1988; Wei Ling et al., 1998; Chein and Chung, 1987; Chung and Troutt, 1988). For small Stokes number droplets, momentum response times are short: $\tau_M = \frac{\rho_p d_p^2}{18\mu_g} \approx 0.03$ s, and dispersion for these droplets is essentially that of fluid particles. At the other extreme for $St = 50$, the momentum response time much longer ($\tau_M \approx 5$ s) and these droplets follow basically a ballistic trajectory.

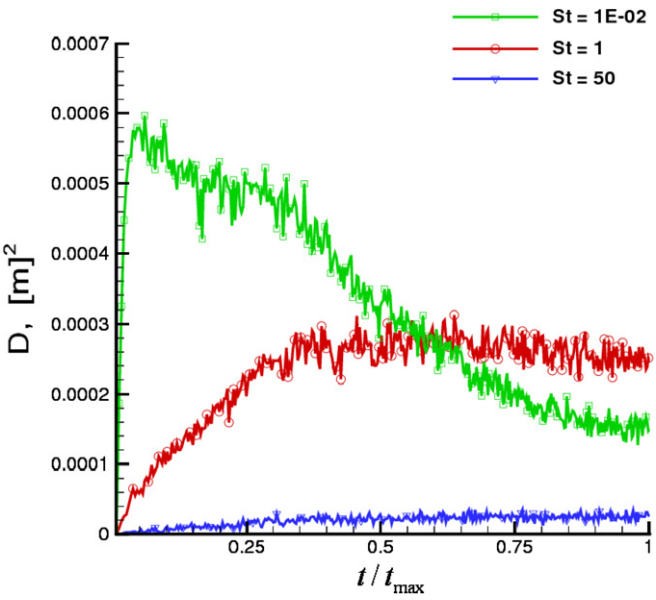

Fig. 10. $D(t)$ vs. time for one-way coupled non-evaporating droplets with $St = 0.01, 1$ and 50.

In addition to the bulk motion, the effects of high frequency gas-phase turbulent fluctuations are also evident in Fig. 10. During the early response time, the effects of SGS turbulence is negligible compared to the mean drag on the droplets due to the bulk motion of the flow. The fluctuations then grow as the shear layer develops with a modeled SGS eddy time scale of $\tau_{SGS} \approx \Omega_m^{-1} = [C_\phi C_\epsilon k^{1/2}/\Delta_f]^{-1} \approx 2.5 \times 10^{-2}\ s^{-1}$. Subgrid scale Stokes numbers based on this time scale are: $St_{SGS} = \tau_p/\tau_{SGS} = \frac{C_\phi C_\epsilon k^{1/2}}{\Delta_f}\rho_p d_p^2 18\mu_g$ and equal 1.25, 30 and 125 for the 100 μm,600 μm, and 3800 μm diameter droplets, respectively. These values are consistent with the observed trends in Fig. 10 with larger fluctuating values for the $St = 0.01$ and $St = 1$ droplets and small fluctuating values for the larger $St = 50$ droplets.

9. Phase-coupling source terms

The phase coupling in a two-phase flow formulation is manifest mathematically through phase-coupling source terms. In more traditional mean-field formulations, (*i.e.* continuum mixture theory, phase-averaged LES, ...*etc.*) the only information available to evaluate source terms is that which is averaged over the computational cell for both phases; that is, information "on the grid" (Pope, 2000; Drew and Passman, 1998; Fox, 2003). The result is that source terms are approximated; *i.e.* $\langle S\rangle_{mean} = f(\langle T_p\rangle, \langle M_p\rangle, \langle U_p\rangle)$ for a given source term, S, that is a function, for example, of particle temperature, mass and velocity. An advantage of the two-phase FDF approach is that particle field information can be used to construct source terms using SGS information taken directly from the Monte-Carlo particles; *i.e.* $\langle S\rangle_{MC} = \langle f(T_p^+, M_p^+, U_p^+)\rangle$. The difference between $\langle S\rangle_{mean}$ and $\langle S\rangle_{MC}$, which defines $\langle S\rangle_{SGS}$, is due to the effects from SGS turbulence plus statistical errors associated with using a finite size ensemble of Monte-Carlo particles. This statistical error scales as $\left(\sqrt{N_p}\right)^{-1}$ and is small relative to S_{SGS} because of the large number of Monte-Carlo particle used (≈ 3.8 million) resulting in statistical errors of approximately 1×10^{-4}.

Fig. 11a shows the time evolution of the normalized stream-wise component of the droplet drag source term, $\langle F_{Du}\rangle_{MC}/\langle F_{Du}(t=0)\rangle_{MC}$, calculated using all of the Monte-Carlo particles in the field. The droplet drag decreases in time because the slip velocities that are initially large decrease as the droplets accelerate. Droplets with larger Stokes number experience larger drag overall because of

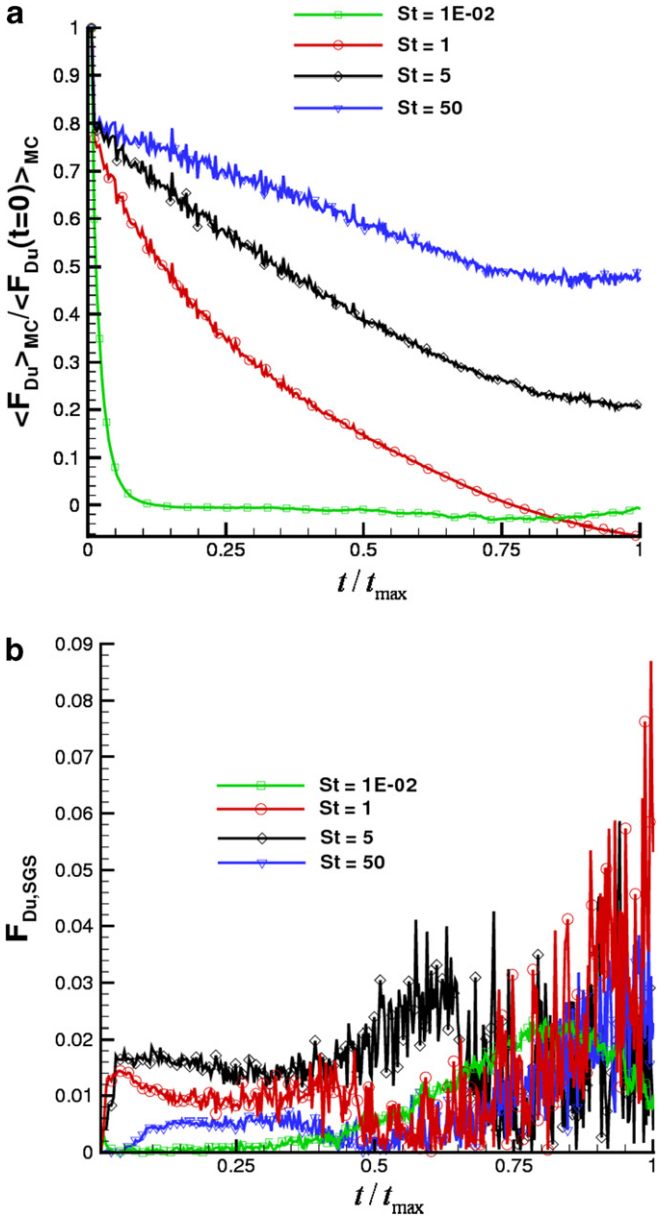

Fig. 11. Normalized spatially averaged stream-wise drag coupling term vs. time calculated from the Monte-Carlo particle field (a) and localized error in the averaged stream-wise drag coupling term vs. time calculated from the particle and mean fields (b).

their slow response to the flow momentum. The smallest droplets with $St = 0.01$ quickly reach dynamic equilibrium with the gas at which time their stream-wise component of drag equilibrates to a constant value near zero. Fig. 11a also shows that the larger droplets exhibit larger variations in $\langle F_{Du}\rangle_{MC}$ compared to the smaller droplets because they cannot adjust as fast to the SGS turbulence fluctuations.

Fig. 11b shows the time evolution of $F_{Du,SGS}(=(\langle F_{Du}\rangle_{mean} - \langle F_{Du}\rangle_{MC}/(\langle F_{Du}(t=0)\rangle_{MC})))$ which is the contribution of the SGS drag source term normalized by the drag at $t = 0$. For the $St > 0.01$ droplets, the contribution of the SGS drag source is between 0.5% and 2% early in the simulation and increases rapidly after $t = 0.75\ t_{max}$. This time corresponds roughly to the eddy turn-over time where the droplets are re-entrained into the high speed laden stream where the SGS turbulent kinetic energy is large.

Fig. 12a shows the time evolution of $\langle F_{Du}\rangle_{mean}/\langle F_{Du}(t=0)\rangle_{mean}$. For this case, the droplet equations are updated using the mean-field values therefore representing a traditional mean-field two-phase flow simulation, *viz.* phase-averaged LES. Comparing Figs. 11a and 12a reveals differences, and these differences are summarized in Fig. 12b representing the compounded error, $\sum F_{Du,SGS}$, that would be introduced if the effects of SGS particle variation were ignored. As shown, the error attains a constant

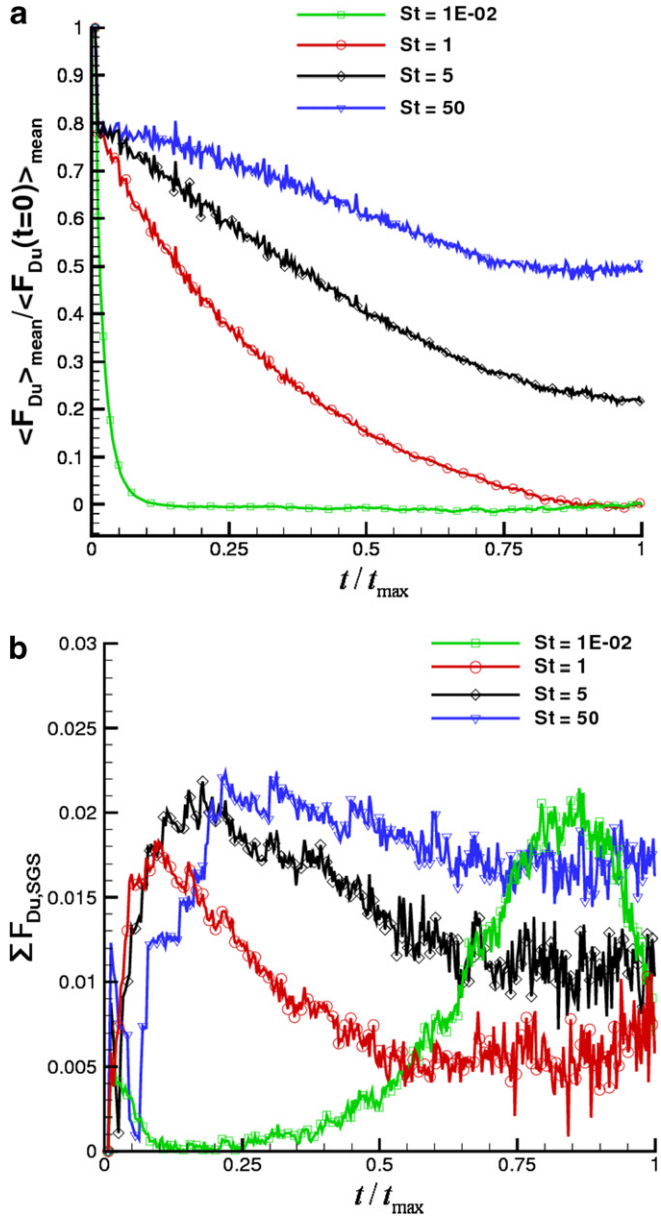

Fig. 12. Normalized spatially averaged stream-wise drag coupling term vs. time calculated from the mean field (a) and compounded error in the averaged stream-wise drag coupling term vs. time calculated from the particle and mean fields (b).

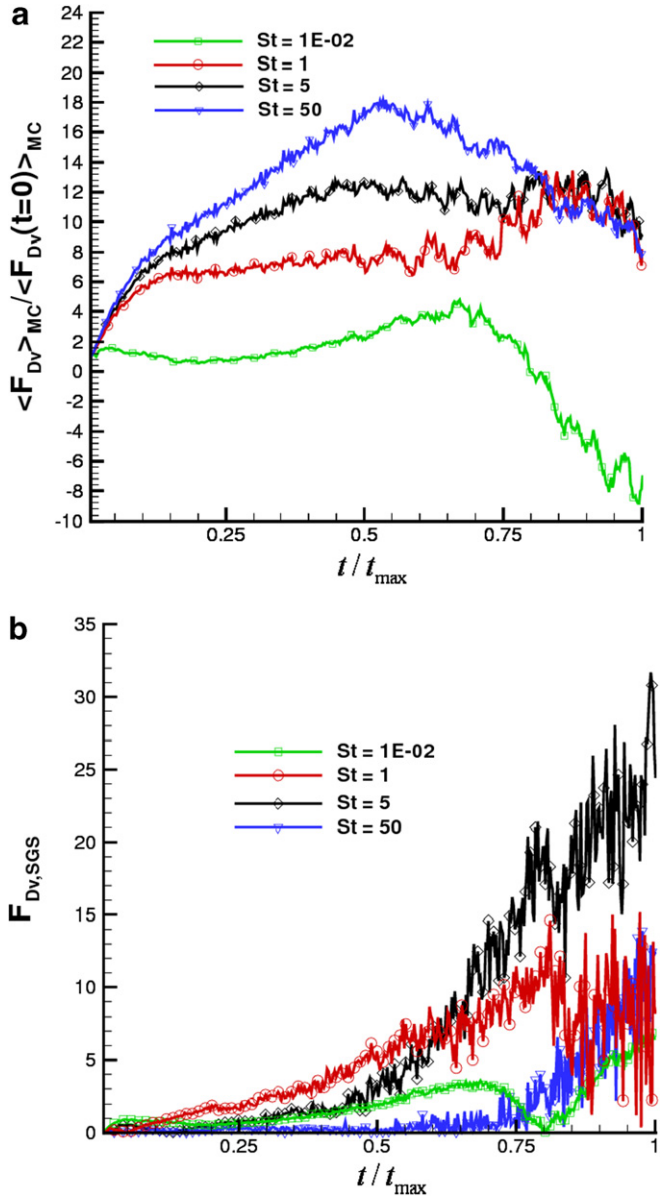

Fig. 13. Normalized spatially averaged cross-stream drag coupling term vs. time calculated from the Monte-Carlo particle field (a) and localized error in the averaged cross-stream drag coupling term vs. time calculated from the particle and mean fields (b).

value between 1 and 2% at $t = t_{max}$ for droplets of $St > 0.01$. For the $St = 0.01$ case, the error grows in time with the maximum occurring at a time corresponding to the eddy turn-over time.

Fig. 13a and b shows the time evolution of the normalized cross-stream component of the momentum source term, $\langle F_{Dv}\rangle_{MC}/\langle F_{Dv}(t=0)\rangle_{MC}$, and $F_{Dv,SGS}$. The normalized $\langle F_{Dv}\rangle_{MC}$ varies over a large range of values because the initial value is small as defined by the initial perturbation velocity in the cross-stream direction. Fig. 13b shows that $F_{Dv,SGS}$ is much larger than $F_{Du,SGS}$ shown in Fig. 11b with peak errors of $\sim 300\%$ for intermediate Stokes number cases. Fig. 14a and b show $\langle F_{Dv}\rangle_{mean}$ and $\sum F_{Dv,SGS}$ where the mean-field information is used to update the droplet equation source terms. Because $\sum F_{Dv,SGS}$ shown in Fig. 13b is large, it is expected that differences between $\langle F_{Dv}\rangle_{MC}$ and $\langle F_{Dv}\rangle_{mean}$ will be large. The is evident by comparing Figs. 13a and 14a as summarized in Fig. 14b.

Fig. 15a and b shows the time evolution of the normalized droplet phase mass loss rate source term, $\langle \dot{M}\rangle_{MC}/\langle \dot{M}(t=0)\rangle_{MC}$, and local error $\dot{M}_{SGS}$. Fig. 15a shows that $\langle \dot{M}\rangle$ increases with increasing Stokes number because of the larger relative slip velocity associated with the larger droplets. The $St = 0.01$ droplets heat up much faster than the larger droplets and quickly attain a temperature close to boiling. At this temperature the mass fraction of water vapor at the droplet surface approaches unity, resulting

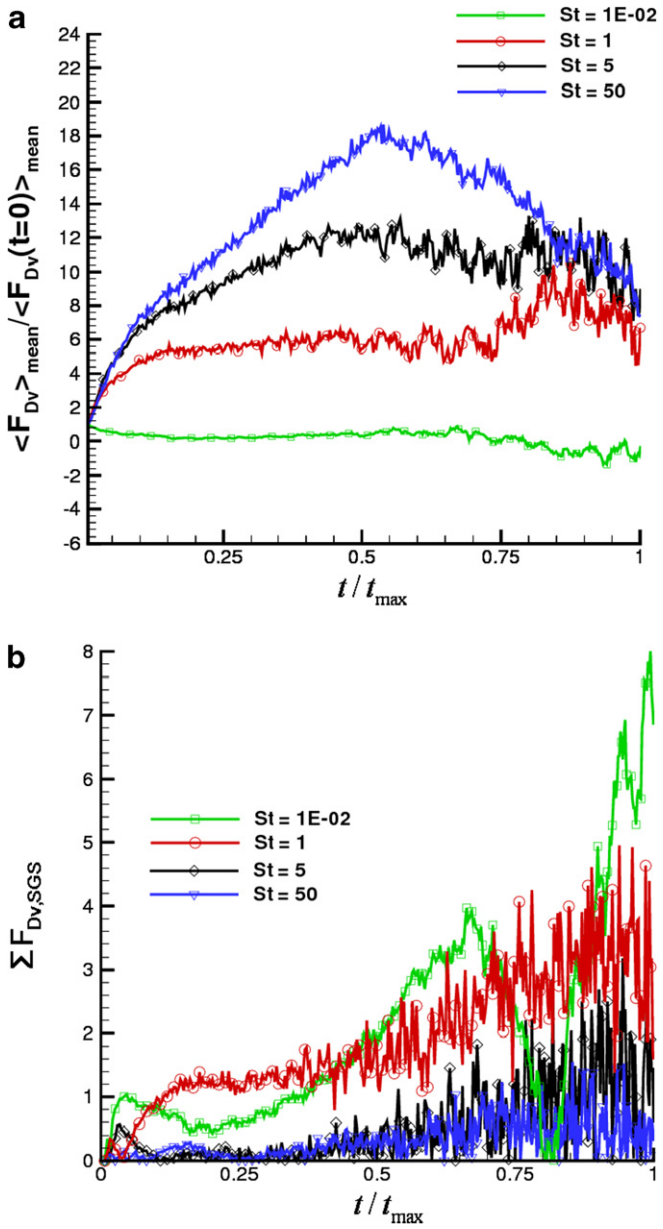

Fig. 14. Normalized spatially averaged cross-stream drag coupling term vs. time calculated from the mean field (a) and compounded error in the averaged cross-stream drag coupling term vs. time calculated from the particle and mean fields (b).

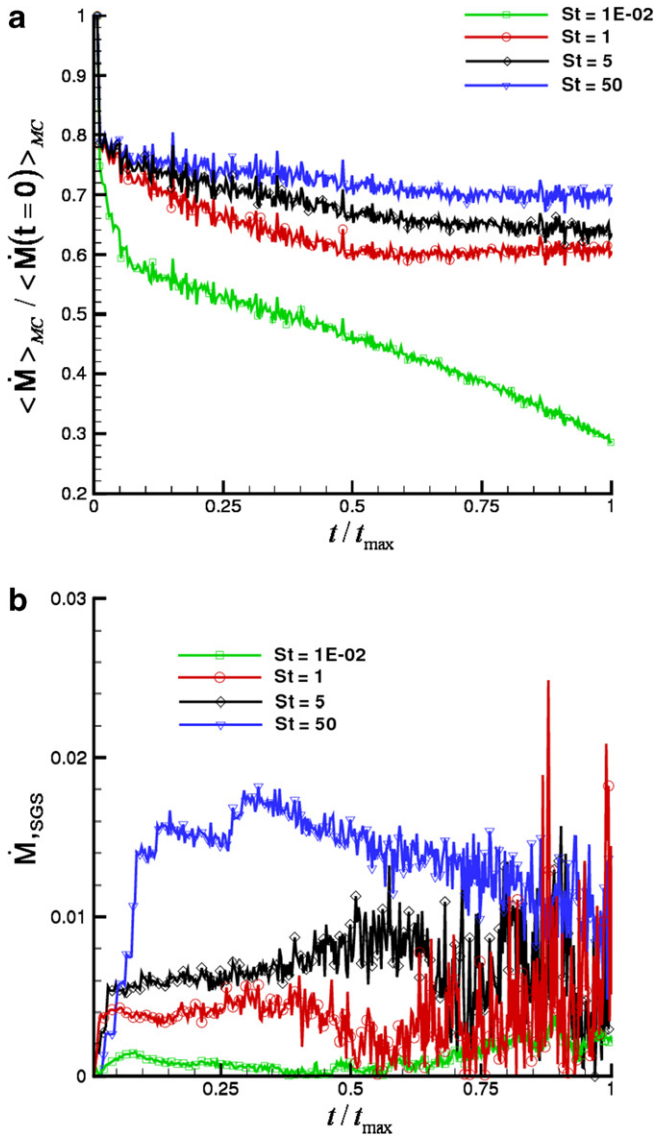

Fig. 15. Normalized spatially averaged mass loss rate coupling term vs. time calculated from the Monte-Carlo particle field (a) and localized error in the averaged mass loss rate term vs. time calculated from the particle and mean fields (b).

in very large values for the mass transfer number, B_M, consequently resulting in the non-linear behavior of the mass loss rate source term observed in Fig. 15a. Fig. 15b shows that $\dot{M}_{SGS}$ has a similar trend as that observed for the drag source terms with largest fluctuations corresponding to the eddy turn-over time. Fig. 16a and b shows the same information as above; that is, $\langle \dot{M} \rangle_{mean}$ and $\sum \dot{M}_{SGS}$, except calculated from the mean field. Fig. 16b shows that the compounded error is relatively small but larger than the local error at later time. For all cases the compounded error increases overall during the course of the simulation.

Fig. 17a and b shows the time evolution of the normalized droplet phase convection source term, $\langle Q_c \rangle_{MC}$, and local error, Qc_{SGS}. Fig. 17a shows that the value of the convection source is dominated by the local slip velocity and

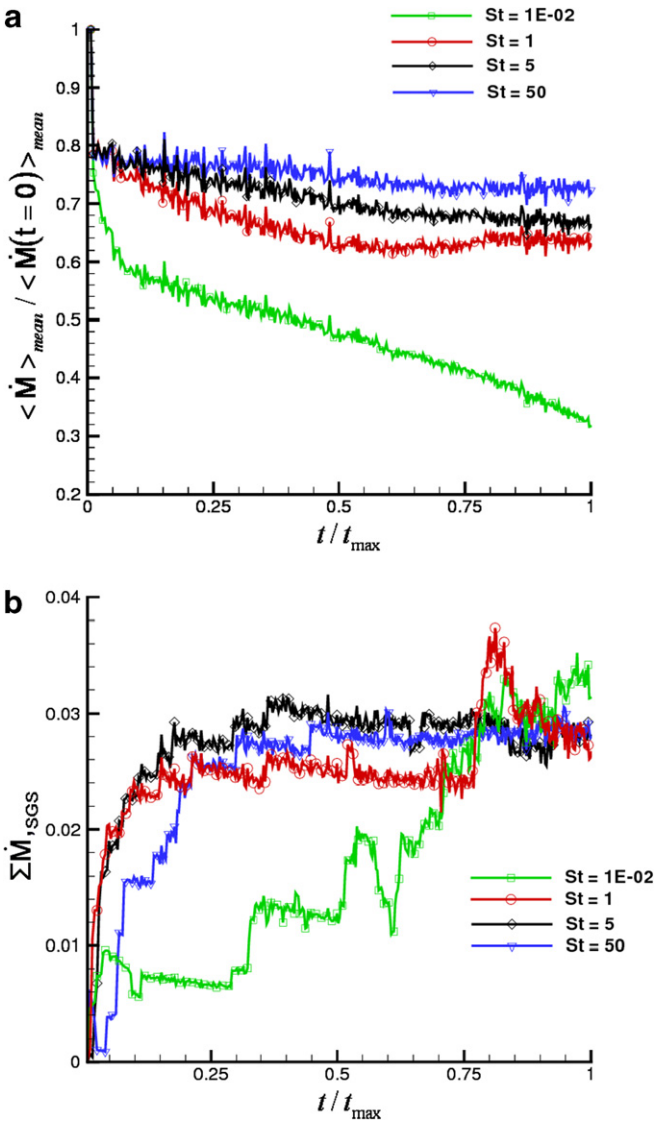

Fig. 16. Normalized spatially averaged mass loss rate coupling term vs. time calculated from the mean field (a) and compounded error in the averaged mass loss rate coupling term vs. time calculated from the particle and mean fields (b).

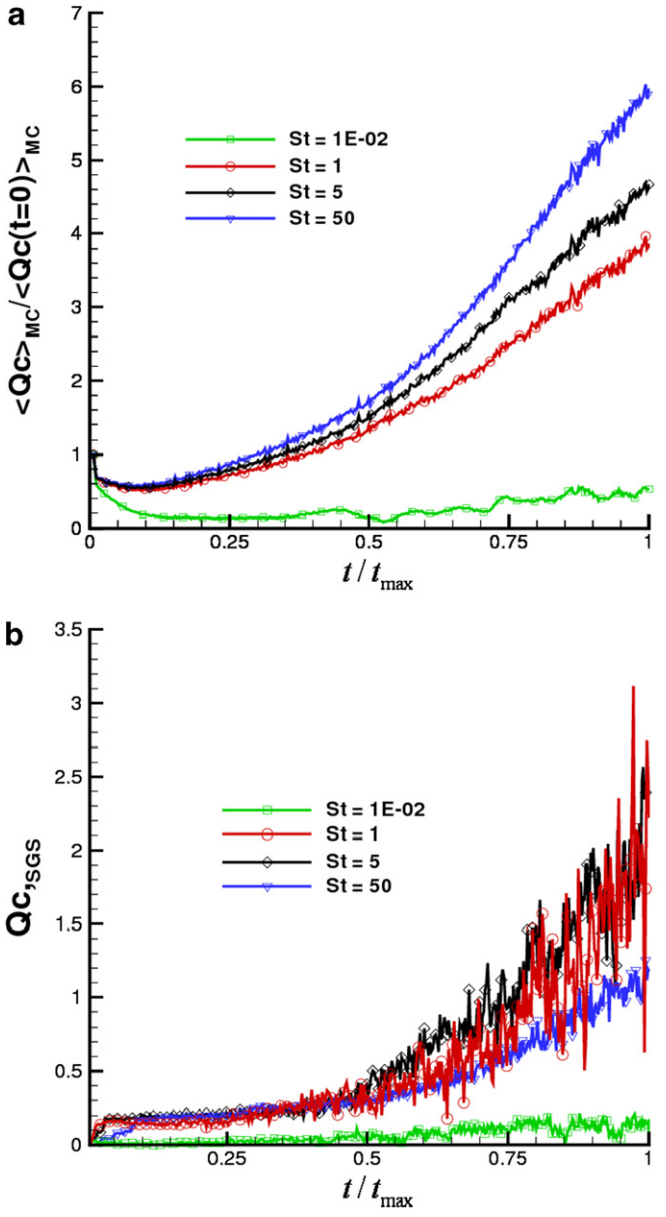

Fig. 17. Normalized spatially averaged convection coupling term vs. time calculated from the Monte-Carlo particle field (a) and localized error in the averaged convection coupling term vs. time calculated from the particle and mean fields (b).

this value increases as the Stokes number increases for the cases $St = 1, 5$ and 50. For the $St = 0.01$ droplets, the convective source quickly decreases as the droplets reach a dynamic equilibrium with the gas and the relative slip goes to zero; *i.e.* see Fig. 11. For these droplets, the convective source term only increases after the droplets have been swept into the hotter gas region and the overall average droplet temperature starts to increase. Consistent with the drag and mass loss rate source terms, the convection source is fairly sensitive to the local turbulent mixing environment as evidenced by the increase in fluctuations in the source terms coinciding with the eddy turn-over time. Fig. 17b shows that the transiently localized error increases

substantially, to as much as 200–300% as the simulation progresses. Again, the sensitivity to SGS turbulence fluctuations is evident by the magnitude of the fluctuations in the error.

Fig. 18a and b shows the same source term time evolution information except the droplet phase equations are updated with the mean-field droplet values and mean-field source terms. Fig. 18b shows that the compounded error increases with increasing Stokes number as time progresses.

Fig. 19a and b shows the time evolution of the ratio of the spatially averaged convection source to evaporation source. Fig. 19a is calculated from the Monte-Carlo particle field whereas Fig. 19b is calculated from the mean field.

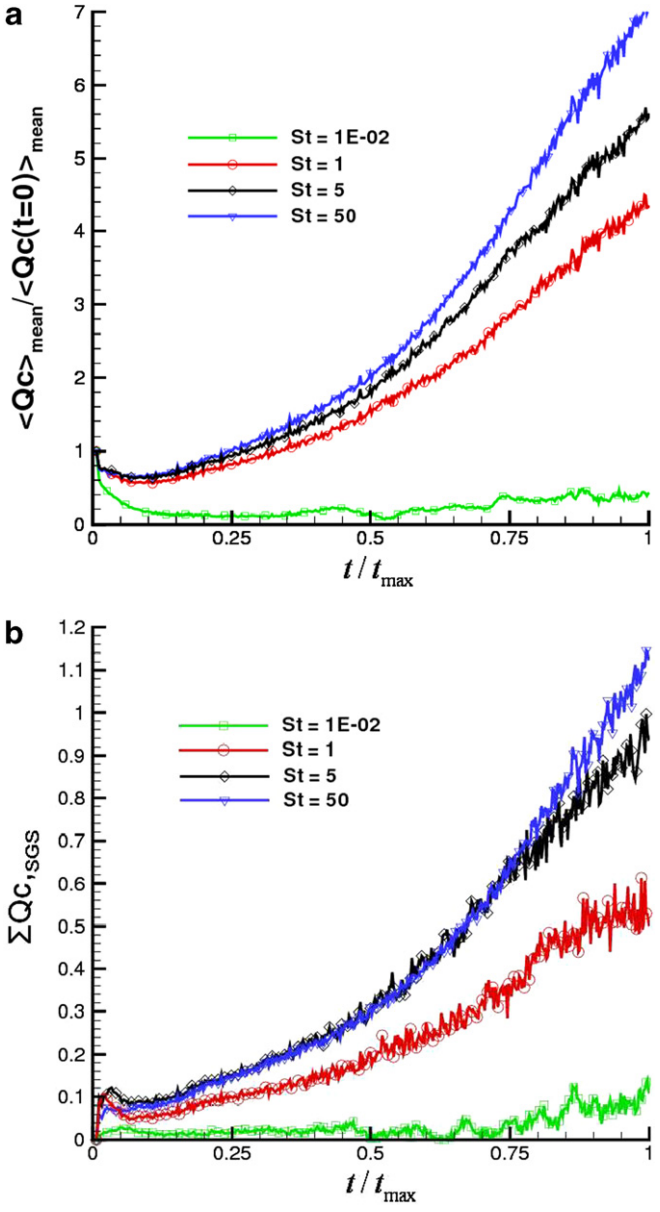

Fig. 18. Normalized spatially averaged convection coupling term vs. time calculated from the mean field (a) and compounded error in the convection coupling term vs. time calculated from the particle and mean fields (b).

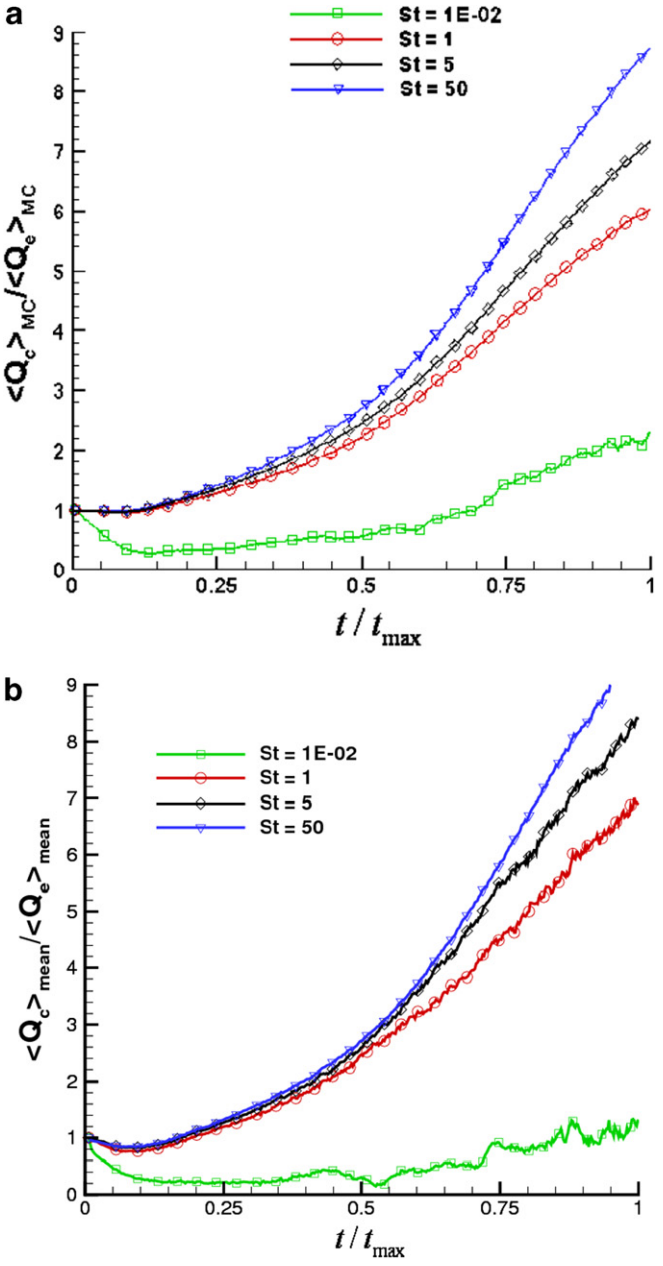

Fig. 19. Normalized spatially averaged convection to evaporation source term vs. time calculated from (a) the Monte-Carlo particle field and (b) the mean field from the computational grid for $St = 0.01, 1, 5$ and 50.

Fig. 19a and b are similar for both cases where the ratio of convection to evaporation source terms are between 6 and 9 for $St \geqslant 1$. For $St = 0.01$ the relative ratio of convection to evaporation heat transfer is close to unity through out the simulation.

10. Conclusions

In this work, the full velocity-scalar filtered mass density function formulation for large eddy simulation of a separated two-phase flow has been applied to a two-phase flow of dilutely dispersed water droplets seeded in

a two-dimensional temporally developing counter-current turbulent mixing layer, for the first time. Closure models for within-phase and phase interface terms for both the dispersed and carrier phases of the flow have been developed and implemented. It has been found that droplets with Stokes number of order unity disperse at a greater rate than gas-phase fluid elements, consistent with other DNS studies and experiments of particulate seeded turbulent free shear flows. It has been found that accounting for the SGS variations in two-way coupled dispersed particle–gas flows is important for accurately calculating phase-coupling source terms. The results in this study confirm the feasibility of a full velocity-scalar FMDF approach for particulate–gas turbulent two-phase flow applications.

Acknowledgments

The authors would like to thank Dr. S.B. Pope (Cornell Univ.) for his advice on implementation of kernel estimation methods, Drs. J.P. Minier (Laboratoire National d'Hydraulique) and J. Pozorski (Polish Academy of Sciences) for their correspondence and advice on the pressure-correction method for full particle based PDF simulations and Dr. T. Drozda (Sandia National Laboratories) for advice on implementation aspects of FDF methods. The authors also thank Mr. Christopher Gately with his assistance running and post-processing the DNS. This research is supported by Sandia National Laboratories (SNL) under Contract No. 64782 and the National Science Foundation under Grant No. CTS-0348110.

References

Anand, M., Hsu, A., Pope, S., 1997. Calculations of swirl combustors using joint velocity-scalar probability density function method. AIAA J. 35, 1143.

Apte, S.V., Gorokhovski, M., Moin, P., 2003. Les of atomizing spray with stochastic modeling of secondary breakup. Int. J. Multiphase Flow 29, 1503–1522.

Bellan, J., 2005. Perspectives on large eddy simulation for sprays: issues and solutions. Atom. Sprays 10, 409–425.

Bilger, R.W., Antonia, R.A., Sreenivasan, K.R., 1976. Determination of intermittency from the probability density function of a passive scalar. Phys. Fluids 18, 1471–1474.

Cao, R., Pope, S., 2003. Numerical integration of stochastic differential equation: weak second-order mid-point scheme for application in the composition pdf method. J. Comput. Phys. 185, 194–212.

Carrara, M.D., DesJardin, P.E., 2006. A filtered density function approach to modeling separated two-phase flows using LES I: mathematical formulation. Int. J. Multiphase Flow 32, 365–384.

Chein, R., Chung, J., 1987. Effects of vortex paring of particle dispersion in turbulent shear flows. Int. J. Multiphase Flow 13, 785.

Chein, R., Chung, J., 1988. Simulation of particle dispersion in a two-dimensional mixing layer. AIChE J. 34, 946–954.

Chung, J., Troutt, T., 1988. Simulation of particle dispersion in a jet. J. Fluid Mech. 186, 199.

Colucci, P.J., Jaberi, F.A., Givi, P., Pope, S.B., 1998. Filtered density function for large eddy simulation of turbulent reacting flows. Phys. Fluids 10, 499–515.

Delarue, B., Pope, S., 1998. Probability density function Monte-Carlo simulation of near-wall turbulent flows. J. Fluid Mech. 357, 141.

DesJardin, P.E., O'Hern, T.J., Tieszen, S.R., 2004. Large eddy simulation and experimental measurements of the near-field of a large turbulent helium plume. Phys. Fluids 16, 1866–1883.

Dopazo, C., O'Brien, E.E., 1976. Statistical treatment of non-isothermal chemical reactions in turbulence. Comb. Sci. Technol. 13, 99–112.

Drazin, P.G., Reid, W.H., 1981. Hydrodynamic Stability. Cambridge University Press, New York, NY.

Dreeben, T., Pope, S., 1992. Non-parametric estimation of mean fields with application to particle methods for turbulent flows. Cornell Technical Report FDA 92-13, Cornell University, Ithaca, NY.

Drew, D., Passman, S., 1998. Theory of Multicomponent Fluids. Springer, New York.

Drozda, T., 2002. Consistency assessment of velocity-scalar filtered density function for large eddy simulation of turbulent flows. M.S. Thesis, Department of Mechanical and Aerospace Engineering, State University of New York at Buffalo, Buffalo, NY.

Fox, R., 2003. Computational Models for Turbulent Reacting Flows. Cambridge, United Kingdom.

Gardiner, C., 1982. Handbook of Stochastic Methods. Springer, New York.

Gicquel, L., Givi, P., Jaberi, F., Pope, S., 2002. Velocity filtered density function for large eddy simulation of turbulent flows. Phys. Fluids 14.

Givi, P., 1989. Model free simulations of turbulent reactive flows. Prog. Energy Comb. Sci. 15, 1–107.

Givi, P., 2003. Subgrid scale modeling in turbulent reacting flows. AIAA Paper AIAA-03-5081.

Goldschmidt, V., Eskinazi, S., 1966. Two-phase turbulent flow in a plane jet. J. Appl. Mech. 33, 1.

Goldschmidt, V., Householder, G., Ahmadi, G., Chuang, S., 1972. Turbulent diffusion of small particles suspended in turbulent jets. Prog. Heat Mass Transfer 6, 487.

Jaberi, F.A., Colucci, P.J., James, S., Givi, P., Pope, S.B., 1999. Filtered mass density function for large eddy simulation of turbulent reacting flows. J. Fluid Mech. 401, 85–121.

Jackson, T.L., Grosch, C.E., 1989. Inviscid spatial stability of a compressible mixing layer. J. Fluid Mech. 208, 609–637.

Janicka, J., Kolbe, W., Kollmann, W., 1979. Closure of the transport equation for the probability density function of turbulent scalar field. J. Nonequilib. Thermodyn. 4, 47–66.

Kataoka, I., 1986. Local instant formulation of two-phase flow. Int. J. Multiphase Flow 12, 745–758.

Lilly, G., 1973. Effect of particle size on eddy diffusivity. Eng. Chem. Fundam. 12, 268.

Lundgren, T.S., 1967. Distribution functions in the statistical theory of turbulence. Phys. Fluids 10, 969–975.

Memmot, V., Smoot, L., 1978. Cold flow mixing rate data for pulverized coal reactors. AIChE J. 24, 466.

Michalke, A., 1964. On the inviscid instability of the hyperbolic tangent velocity profile. J. Fluid Mech. 19, 543–556.

Miller, R., Bellan, J., 1999. Direct numerical simulation of a confined three-dimensional gas mixing layer with one evaporating hydrocarbon-droplet-laden stream. J. Fluid Mech. 384, 293–338.

Miller, R., Bellan, J., 2000. Direct numerical simulation and subgrid analysis of a transitional droplet laden mixing layer. Phys. Fluids 12, 650–671.

Minier, J., Peirano, E., 2001. The pdf approach to turbulent polydisperse two-phase flows. Phys. Rep. 352, 1–214.

Minier, J., Pozorski, J., 1995. Analysis of a pdf model in a mixing layer case. In: Tech. Rep. 10th Symposium of Turbulent Shear Flows, The Pennsylvania State University, University Park, PA.

Minier, J., Pozorski, J., 1999. Wall-boundary conditions in probability density function methods and application to a turbulent channel flow. Phys. Fluids 11, 2632–2644.

O'Brien, E.E., 1980. The probability density function (PDF) approach to reacting turbulent flows. In: Libby, P.A., Williams, F.A. (Eds.), Turbulent Reacting Flows. Springer-Verlag, Heidelberg, pp. 185–218.

Oefelein, J.C., Yang, V., 1996. Simulation of high-pressure spray field dynamics. In: Recent Advances in Spray Combustion: Spray Atom-

ization and Drop Burning Phenomena, Progress in Astronautics and Aeronautics, vol. 2, pp. 263–304.

Okong'o, N., Bellan, J., 2004. Consistent large-eddy simulation of a temporal mixing layer laden with evaporating drops. Part 1. Direct numerical simulation, formulation and a priori analysis. J. Fluid Mech. 499, 1–47.

Pope, S.B., 1976. The probability approach to modeling of turbulent reacting flows. Comb. Flame 27, 299–312.

Pope, S.B., 1985. PDF methods for turbulent reacting flows. Prog. Energy Comb. Sci. 11, 119–192.

Pope, S., 1994. On the relation between stochastic lagrangian models of turbulence and second-moment closures. Phys. Fluids 6, 973.

Pope, S., 2000. Turbulent Flows, second ed. Cambridge University Press, Cambridge, UK.

Radhakrishnan, K., Hindmarsh, A.C., 1993. Description and use of LSODE, the Livermore Solver for Ordinary Differential Equations. Tech. Rep. UCRL-ID-113855, Lawrence Livermore National Laboratory, Livermore, CA.

Ranz, W.E., Marshall, W.R., 1952. Evaporation from drops. Chem. Eng. Prog. 48, 141–173.

Rhodes, P.R., 1975. A probability distribution function for turbulent flows. In: Murthy, S.N.B. (Ed.), Turbulent Mixing in Non-Reactive and Reactive Mixing. Plenum Press, New York, NY, pp. 235–241.

Rogallo, R.S., Moin, P., 1984. Numerical simulation of turbulent flow. Ann. Rev. Fluid Mech. 16, 99–137.

Sheikhi, M.R.H., Drozda, T.G., Givi, P., Pope, S.B., 2003. Velocity-scalar filtered density function for large eddy simulation of turbulent flows. Phys. Fluids 15, 2321–2337.

Sirignano, W.A., 2005. Volume averaging for the analysis of turbulent spray flows. Int. J. Multiphase Flow 31, 675–705.

Smagorinsky, J., 1963. General circulation experiments with the primitive equations. I. The basic experiment. Month. Weather Rev. 91, 99–164.

Squires, K.D., Eaton, J., 1990. Particle response and turbulence modification in isotropic turbulence. Phys. Fluids A 2, 1191–1203.

Wei Ling, J.N., Chung, J., Crowe, C., Troutt, T.R., 1998. Direct numerical simulation of a three-dimensional mixing layer with particle dispersion. J. Fluid Mech. 358, 61–85.

Wen, F., Kamalu, N., Chung, J., Crowe, C., Troutt, T.R., 1992. Particle dispersion by vortex structure in plane mixing layers. J. Fluids Eng. 114, 657–666.

Xu, J., Pope, S., 1999. Assessment of numerical accuracy of pdf/Monte Carlo methods for turbulent reacting flows. J. Comput. Phys. 152, 192–230.

Yuu, S., Yasukouchi, N., Hirosawa, Y., Jotaki, T., 1978. Particle turbulent diffusion in a dust-laden round jet. AIChE J. 24, 509.

Zhou, X.Y., Pereira, J.C.F., 2000. Large eddy simulation (2d) of a reacting plane mixing layer using filtered density function closure. Flow Turb. Comb. 64, 279–300.

Zhu, M., 1996. Modeling and simulation of spray combustion with pdf methods. Ph.D. Thesis, University of Cambridge, Cambridge.

Zhu, M., Bray, K.N.C., Rumberg, O., Rogg, B., 2000. PDF transport equations for two-phase reactive flows and sprays. Comb. Sci. Technol. 122, 327–338.